Supplementary material for "Particle flux dynamics amplify marine carbon cycle differences between climate states"

Markus Adloff[1,2], Frerk Pöppelmeier[1,2], Ashley Dinauer[1,2], Charlotte Laufkötter[1,2], and Fortunat Joos[1,2]

[1]Climate and Environmental Physics, Physics Institute, University of Bern, Switzerland
[2]Oeschger Centre for Climate Change Research, University of Bern, Switzerland

1 Implementation of the implicit version of MSPACMAM

MSPACMAM (Dinauer et al., 2022) calculates vertical profiles of organic (POC), calcite, aragonite, and opal (OPAL) particles through depth-by-depth temporal integration of particle losses and downward fluxes until a dynamic equilibrium is achieved. This approach requires much shorter time steps than those of Bern3D (∼3 days), making its direct implementation costly. To reduce computational cost and increase numerical stability, we devised an implicit scheme which estimates the dynamic equilibrium based on primary production, particle sinking speed and environmental conditions in the water column.

Our model operates on a 3D grid with i and j indicating longitude and latitude of the center of a grid cell. k' indicates the depth of the upper boundary of the grid cell k, and $k'+1$ indicates the lower boundary of the grid cell . $dz(k) = z(k'+1) - z(k')$ is the thickness of cell k. In the following i, j are omitted to ease notation. Variables are specific for depth (k), size class (l) and particle component (m; POC,calcite,aragonite,opal):

$f0(0,l,m)$: export flux out of euphotic zone (mol/(m^2/s))
$v(k,l)$: mean sinking speed in box k (m/s) (approximated by $v(k',l)$)
$dt_P(k,l) = dz(k)/v(k,l)$: average time particle is spending in box k (s) (approximated by $dz(k)/v(k',l)$
$r_P(k',l,m)$: particle remineralization/dissolution rate (1/s) at depth k'
dt: model time step (s)

The 1-dimensional equation for the divergence of a particle flux can be written as $\frac{\partial c}{\partial t} + \frac{\partial f}{\partial z} = 0$, with particle concentration c, particle velocity v, and particle flux $f = c \cdot v$. For particles dissolving with rate r_P, the temporal change in particle concentration is: $\frac{\partial c}{\partial t} = -r_P \cdot c$. It follows $\partial f = r_P \cdot c \cdot \partial z = r_P \cdot (c \cdot v) \cdot \partial z / v$. Where $\partial z / v$ is the time, dt_P, the particles require for travelling distance ∂z. We get $\partial f = r_P \cdot f \cdot dt_P$ and this equation is transferred to our model grid. We can then calculate the degradation rate in box k between depth k' and k'+1 either relative to the input f(k',l,m), or output f(k'+1,l,m), of the box, or a mix of the two, resulting in three different approaches to derive f(k'+1,l,m) from f(k',l,m):

Scheme 'k1':

$$rP(k',l,m) \cdot dtP(k,l) = \frac{f(k',l,m) - f(k'+1,l,m)}{f(k',l,m)} \tag{S1.1}$$

$$f(k'+1,l,m) = f(k',l,m) \cdot (1 - rP(k',l,m) \cdot dtP(k,l)) \tag{S1.2}$$

Scheme 'k2':

$$rP(k',l,m) \cdot dtP(k,l) = \frac{f(k',l,m) - f(k'+1,l,m)}{f(k'+1,l,m)} \tag{S1.3}$$

$$f(k'+1,l,m) = f(k',l,m) \cdot (\frac{1}{1 + rP(k',l,m) \cdot dtP(k,l)}) \tag{S1.4}$$

Scheme 'k12':

$$rP(k',l,m) \cdot dtP(k,l) = \frac{f(k',l,m) - f(k'+1,l,m)}{\frac{1}{2}f(k',l,m) + \frac{1}{2}f(k'+1,l,m)} \tag{S1.5}$$

$$f(k'+1,l,m) = f(k',l,m) \cdot \frac{1 - \frac{1}{2}rP(k',l,m) \cdot dtP(k,l)}{1 + \frac{1}{2}rP(k',l,m) \cdot dtP(k,l)} \tag{S1.6}$$

We chose the second approach because it is numerically stable: As $rP(k',l,m)$ and $dtP(k,l,m)$ are always positive, the denominator is always ≥ 1 in the second approach, and f cannot grow with depth irrespective of the absolute values of $rP(k',l,m)$ and $dtP(k,l,m)$, and f cannot become negative. k2 is also the scheme which produces the smallest errors compared to the explicit scheme, implemented offline and evaluated on the vertical Bern3D grid (SI Fig S2.8 for an examplary location in the South Pacific).

Following Dinauer et al. (2022) particle sinking speeds depend on the viscosity and density of water, as well as the density and composition (relative portion of organic matter, calcite, aragonite and opal) of the sinking particle mix in each size fraction. The loss of particles in a given box, in turn, depends on the time a particle spends in the box (dt_P), dictated by the sinking speed and the environmental conditions in that box that determine the remineralization and dissolution rates (r_P). As in our scheme we propagate the particle flux stepwise from the bottom of the euphotic zone (at a uniform depth of 75 m in the model) to the sea floor, the particle composition is initially only known at the upper boundary of a given grid cell. Hence, we chose to evaluate the sinking speed and particle loss rate in each grid cell at its upper boundary. Below the thermocline, environmental conditions, and consequently seawater density and viscosity and particle decay rates, change slowly with depth and particle loss rates are less sensitive to the exact depth at which they are evaluated. Within the thermocline, however, particle losses vary largely if they are determined at the upper cell boundary or in the centre of the cell. This discretization error is particularly large for the slowly sinking small particles. In an effort to reduce the error in the upper water column, we additionally evaluate the particle composition and loss terms at mid-depth of the first grid box below the euphotic zone, and consequently use this

composition to calculate the particle composition at its lower boundary, effectively splitting this box into two for the calculation of particle fluxes. This approach strongly reduces the discretization error in the small size fraction, while introducing a smaller error in the large particle fraction (see SI Fig. S2.8).

The advantage of the new implicit scheme is its reduced computational cost by avoiding the explicit simulation of the particles incrementally sinking through the water column, while keeping spatial and temporal variations in dissolution rates and sinking speeds. By choosing implicit scheme K2 with doubled vertical resolution directly below the euphotic zone, we minimized the error that results from using an implicit rather than explicit particle flux propagation.

Bern3D adjusts the respiration rate of organic particles in oxygen minimum zones to account for anaerobic respiration due to denitrification by varying the local exponent of the Martin Curve (Battaglia and Joos, 2018). Organic particle respiration in Dinauer et al. (2022) is oxygen-dependent but does not contain an anaerobic respiration term. We added this effect by applying the Martin Curve with reduced exponent from Battaglia and Joos (2018) to the fraction of organic particles that is not respired aerobically, as determined by the new scheme.

We also added a dependence on POC remineralization to the dissolution rates of calcite or aragonite following Liang et al. (2023) to allow for dissolution above the saturation horizon. Specifically, we follow the 'Model 3' of Liang et al. (2023) by calculating the 'net dissolution rate' $rCaCO3_{net}$ as the sum of the saturation state-dependent dissolution rate $rCaCO3_{\Omega}$ of carbonate (we keep using the one used in Dinauer et al. (2022)) and the respiration-dependent dissolution rate $rCaCO3_{resp} = x(f_{POP}(k) - f_{POP}(k+1))^m$, where x and m are tunable parameters. To reduce the overall number of tunable parameters in our tuning ensemble, we decided to set x = 1 and only tune the exponent m, since the scaling effect of x can also be achieved by varying m. Hence, our equations for the dissolution rates of the two carbonate species calcite and aragonite are:

$$rCaCO3_{net,calcite} = rCaCO3_{\Omega,calcite} + (f_{POP}(k') - f_{POP}(k'+1))^{m_{calcite}} \tag{S1.7}$$

$$rCaCO3_{net,aragonite} = rCaCO3_{\Omega,aragonite} + (f_{POP}(k') - f_{POP}(k'+1))^{m_{aragnonite}} \tag{S1.8}$$

We kept the dependence of the saturation state-dependent dissolution rates on particle size as in Dinauer et al. (2022), but assume that respiration-dependent dissolution affects carbonate independently of particle size. The export production routine of Bern3D does not differentiate between calcite and aragonite. Hence, for the new particle flux scheme we split the Bern3D carbonate export flux into calcite and aragonite export by introducing the new constant and spatially uniform tuning parameter e_{arag}, which determines the proportion of the carbonate export flux that is aragonite.

Since Bern3D does not track seawater viscosity, we calculated it dynamically at the upper boundary of each grid cell following Sharqawy et al. (2010).

A list of fixed parameters in the new module is provided in table S1.1.

Table S1.1. Fixed parameters in the new scheme, adopted from Dinauer et al. (2022).

Parameter	Unit	Value	Description
r_{lg}	cm	0.025	Radius of large particles
T_{ref}	°C	15	Reference Temperature for POC remineralization
SSA_{calcSm}	m^2/mol	1040.0	Specific surface areas of small calcite particles
SSA_{calcLg}	m^2/mol	430.0	Specific surface areas of large calcite particles
SSA_{arag}	m^2/mol	217.0	Specific surface areas of aragonite particles
$k_{calcUpEx}$	unitless	-10.3	Exponent for rate constant (mol/($m^2 \cdot$ s)) for calcite dissolution (Ω>0.8)
n_{calcUp}	unitless	0.11	Reaction order for calcite dissolution (Ω>0.8)
$k_{calcLowEx}$	unitless	-6.8	Exponent for rate constant (mol/($m^2 \cdot$ s)) for calcite dissolution (Ω<0.8)
$n_{calcLow}$	unitless	4.7	Reaction order for calcite dissolution (Ω<0.8)
k_{arag}	mol/($m^2 \cdot$ s)	6.1164e-10	Rate constant for aragonite dissolution
n_{arag}	unitless	1.37	Reaction order for aragonite dissolution
ρ_{OM}	g/cm^3	1.06	Density of solid organic matter
ρ_{CaCO_3}	g/cm^3	2.71	Density of solid $CaCO_3$
ρ_{Opal}	g/cm^3	2.10	Density of solid opal
MW_C	g/mol	12.0	Molecular weight of carbon
MW_{CaCO_3}	g/mol	100.0	Molecular weight of carbonate
MW_{SiO_2}	g/mol	60.0	Molecular weight of opal
α_{OMC}	g/g	2.7	Mass ratio of organic matter to carbon

2 Implementation of the new Fe cycle

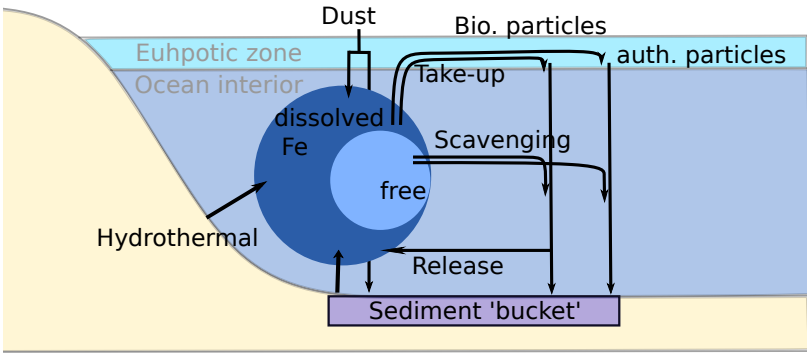

Figure S1.1. Schematic of the new Fe cycle in Bern3D, which is based on the one described in Somes et al. (2021) with authigenic Fe cycling following Tagliabue et al. (2023).

Alongside the new particle flux profiles, we updated the Fe chemistry in Bern3D. A conceptual depiction of the new Fe scheme is shown in Fig. S1.1, including hydrothermal, dust and dynamic sedimentary Fe sources to the ocean and Fe removal by biotic uptake, authigenic Fe particle formation and scavenging (equation 4).

Following Parekh et al. (2004), only the 'free' fraction of Fe, i.e. the fraction that is not bound to organic ligands, can be scavenged by the modeled particle fluxes. For simplicity, we do not trace ligand concentrations over space and time. Instead, we use the approach by Völker and Tagliabue (2015) and estimate the ligand concentration at every time step and grid cell from the concentration of dissolved organic C (DOC) and organic matter degradation. Due to missing tracers, Somes et al. (2021) used apparent oxygen utilization (AOU) to estimate degradation rates. We chose instead to calculate ligand concentrations (lig) based on the concentration of local remineralised carbon (i.e. the difference between total regenerated DIC and DIC released from $CaCO_3$ dissolution, $bgcREM$) given the good reproduction of measured ligand distribution that Völker and Tagliabue (2015) achieved by linking ligands to actual remineralization rates and that AOU is an imperfect metric for remineralization (Cliff et al., 2021):

$$lig = bgcligREM \cdot bgcREM^{0.8} + bgcligDOC \cdot DOC^{0.8} \tag{S1.9}$$

bgcligREM (2.2 μmol/m^3 (mol/m^3)$^{-0.8}$) and bgcligDOC (50 μmol/m^3 (mol/m^3)$^{-0.8}$) are globally constant parameters. Based on the ligand concentration, we then derive the concentration of free Fe and colloidial Fe following Parekh et al. (2004); Nickelsen et al. (2015):

$$A = 1. + ligstab \cdot (lig - Fe) \tag{S1.10}$$

$$Fe_{free}(i,j,k) = (-A + \sqrt{A^2 + 4 \cdot ligstab \cdot Fe})/(2 \cdot ligstab) \tag{S1.11}$$

$$cFe = 0.5 \cdot (Fe - Fe_{free}) \tag{S1.12}$$

where Fe is the available Fe concentration (total concentration minus the Fe used up in primary production in the same time step), Fe_{free} is free Fe, cFe is colloidial Fe and $ligstab$ is a globally constant parameter. Colloidal Fe is removed by authigenic particle coagulation and export based on the PISCES-QUOTA model Kwiatkowski et al. (2018); Tagliabue et al. (2023). Colloidal Fe is calculated in-situ as a fixed fraction of ligand-complexed Fe (Aumont et al., 2015). Following the parameterisations for aggregation (aggregation rate agg in mol dm^{-3} s^{-1}) and auto-coagulation (auto-coagulation rate $auto$ in mol m^{-}3 s^{-1}) in Tagliabue et al. (2023), a portion of this colloidal Fe pool is incorporated into authigenic particles. Similar to the treatment of biogenic particles in Bern3D, authigenic particles are not tracked across time steps and move only downward through the water column.

$$agg = (12.0 \cdot 0.3 \cdot DOC + 9.05 \cdot C_{POM,small}) \cdot shear \tag{S1.13}$$

$$+(2.49 \cdot C_{POM,small}) + (127.8 \cdot 0.3 \cdot DOC \tag{S1.14}$$

$$+725.7 \cdot C_{POM,small}) \tag{S1.15}$$

$$+(1.940 * shear + 1.37) \cdot C_{POM,large} \tag{S1.16}$$

$$auto = \frac{0.1}{86400} \cdot cFe^4/(cFe^4 + (2 \cdot 10^{-6})^4) \tag{S1.17}$$

$$aPFe_{auth} = (agg \cdot 10^{-3} + auto) \cdot cFe \tag{S1.18}$$

Where $C_{POM,small}$ and $C_{POM,large}$ are amounts of carbon in small and large organic particles and $shear$ is depth-dependent ($shear$ = 1.0 above 100 m and $shear$ = 0.01 below). $aPFe_{auth}$ is the rate at which authigenic particulate Fe particles form (with unit mol m^{-3} s^{-1}).

For simplicity, we do not differentiate between different size classes of authigenic particles and assume that the sinking speed of authigenic particles is the same as that of the biogenic particle mix.

$$Fe_{scavenged} = FeSigPOC \cdot x_{O2} \cdot POM + FeSigIno \cdot x_{O2} \cdot (CaCO_3 + Opal) + FeSigAuth \cdot x_{O2} \cdot PFe_{authigenic} \tag{S1.19}$$

The Fe scavenging flux Fe_{scav} is scaled to local particle concentrations P using separate, tunable factors ($FeSig$) for organic and inorganic particles ($FeSigPOC$ and $FeSigIno$, respectively (equation 19, tuned values are given in Table S1.3), with a

choice between the empirical models by Moore and Braucher (2008), accounting for scavenging by organic particles, $CaCO_3$ and opal, and Nickelsen et al. (2015) which only considers scavenging by organic particles. We added an O_2 dependence to the scavenging fluxes by multiplying with the unitless factor x_{O2}, following the PISCES-QUOTA model (Kwiatkowski et al., 2018).

$$x_{O2} = max(10^{-3}, (1.0 - e^{-2 \cdot O_2/(100 \cdot 10^{-3})})) \tag{S1.20}$$

Authigenic particles also scavenge Fe as they sink, with a tunable scaling factor $FeSigAuth$. For each vertical grid cell column and time step, we track the amount of Fe scavenged by organic, inorganic and authigenic particles. This Fe is released back into the water column proportionately to particle remineralization/dissolution.

(a) Hydrothermal

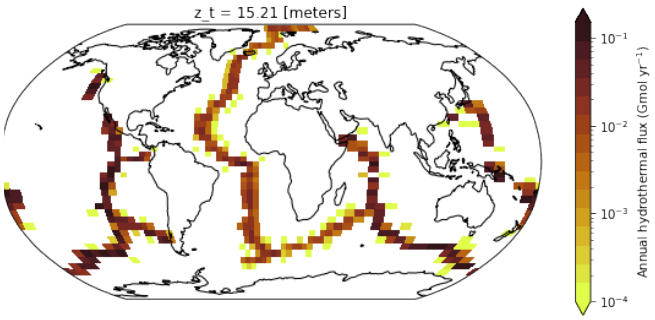

(b) Dust

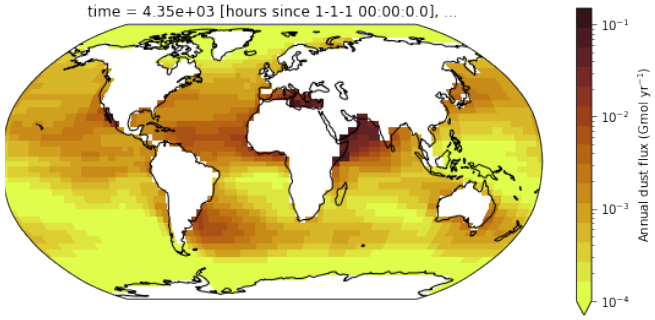

Figure S1.2. Prescribed Fe input fields from hydrothermal vents (see text) and dust based on Mahowald et al. (2006)

The sedimentary Fe flux $inFe_{sediment}$ is tied to the sedimentary POM oxidation rate (Dale et al., 2015), which is explicitly calculated if the sediment module is used, or estimated based on the POM flux reaching the sediments following Floegel et al. (2011); Niemeyer et al. (2017):

$$Cox = (C_{POM} - 0.14 \cdot C^p_{POM}) \tag{S1.21}$$

$$inFe_{sediment} = bgcfesedmax \cdot tanh(Cox/O_2) \tag{S1.22}$$

Where C_{POM} is the carbon reaching sediments in particulate organic matter, p is an exponent that is set to 1.11 for locations with less than 1000 m water depth and 1.05 below.

The cited studies prescribe a maximum rate of sedimentary Fe release but do not track the Fe available for release in the sediments. We intend to use the Fe scheme in Bern3D for simulating glacial timescales. On these time scales a potentially unlimited sedimentary Fe supply can result in positive feedback loops, whereby increased organic carbon supply to the sediments

increases sedimentary Fe release, which, if upwelled, re-enforces production. We chose to implement a simplified sedimentary Fe reservoir in each sediment column to avoid run-away feedbacks due to productivity change. This reservoir accumulates the fraction of aolian Fe that is not dissolved in the surface ocean, as well as all Fe incorporated into organic particles that fall onto the seafloor and any scavenged Fe that does not get released back into the water column. If the calculated release rate of sedimentary Fe exceeds the amount stored in the reservoir, the release is limited to the available Fe.

A list of fixed parameters in the new module is provided in table S1.2.

Table S1.2. Fixed parameters in the new scheme.

Parameter	Unit	Value	Description
ffedust	unitless	0.016	Scaling of aeolian Fe flux
fesol	unitless	0.02	Solubility of Fe in dust
fefrac	unitless	0.035	Fraction of Fe in dust
ffehydro	unitless	1.205	Scaling of hydrothermal Fe flux
LigMin	mol/m^3	0.5e-6	Minimum ligand concentration
LigStab	(mol/m^3)$^{-1}$	1.e8	Fe-Ligand stability constant
Fesed$_{max}$	mol/m^2	46.9e-11	Maximum Fe flux from sediments
Febucket$_{init}$	mol	1e2	Initial size of Fe bucket in each benthic grid box
ligREM	(mol/m^{-3})/(mol/m^{-3})$^{-0.8}$	2.2e-6	Relationship between remineralized carbon and ligands
ligDOC	(mol/m^{-3})/(mol/m^{-3})$^{-0.8}$	0.5e-4	Relationship between DOC and ligands
freefemax	mol/m^{-3}	1e-6	Maximum Fe$_{free}$ concentration

3 Model tuning

The newly implemented schemes contain several parameters that we tuned to achieve steady state spatial distributions of biochemical species that are consistent with observations. Specifically, these include properties of the biogenic particles and the speed of remineralization in the particle flux scheme, the dependence of carbonate dissolution on POC remineralization, Fe scavenging, as well as the aragonite fraction of the carbonate export flux and the ratio of Fe to phosphate uptake during primary production. The full list of tuned parameters, their ranges and optimal values are shown in table S1.3.

Table S1.3. Tuning parameters

Parameter	Unit	Range	New Default	Description
r_{sm}	cm	0.002 - 0.003	0.0023	Radius of small particles
ϕ_{sm}	unitless	0.0 - 0.6	0.351	Porosity of small particles
ϕ_{lg}	unitless	0.95 - 0.99	0.953	Porosity of large particles
k_{POC}	s^{-1}	$2e^{-6}$ - $3.819e^{-6}$	$2.8266e^{-6}$	POC remineralization rate constant
k_{O2}	mol m^{-3}	0.001 - 0.02	0.0073	Half-Saturation constant for oxygen uptake
aE	$^{\circ}C^{-1}$	0.04 - 0.2	0.155	Exponent for temperature modification of remineralization
e_{arag}	unitless	0.2 - 0.25	0.217	Aragonite fraction of carbonate export
R_{mcal}	unitless	0.47 - 0.51	0.48	Coefficient relating calcite dissolution to remineralization
R_{marag}	unitless	0 - 0.1	0.057	Coefficient relating aragonite dissolution to remineralization
FeSigPOC	unitless	0 - 2	0.955	Fe scavenging factor for organic particles
FeSigIno	unitless	0 - 1	0.288	Fe scavenging factor for inorganic particles
FeSigAuth	unitless	0 - 0.01	0.009	Fe scavenging factor for authigenic Fe particles
bgcaggpar	unitless	0 - 0.0001	3.02e-8	Scaling factor for authigenic Fe particle aggregation
redfep	unitless	$3e^{-4}$ - $5.8e^{-4}$	$3.5e^{-4}$	Fe:PO_4 of organic export

For computational efficiency, we refined the tuning parameters iteratively and thereby reduced the overall number of simulations run. In total we ran three tuning ensembles with 200 members each. Each simulation equilibrates the model (atmosphere-ocean only) over 10 kyr to pre-industrial orbital parameters and greenhouse gas concentrations with fixed atmospheric CO_2.

We evaluated the root mean square error of the 3D-fields of DIC, ALK, O_2, PO_4^{3-}, SiO^{2-}, Fe, $DI^{13}C$ and $DI^{14}C$ relative to the respective observational fields from WOA 2018, GLODAP v2 and GEOTRACES 2021 v2 between each member of the tuning ensembles. We further assessed the carbon cycle disequilibrium, which emerges from the marine carbon cycling and is masked by the atmospheric CO_2 restoring in our initial tuning ensemble, by continuing each simulation for 10 kyr without CO_2 restoring. The parameter sets which yielded the five lowest cumulative errors were then forced with the radiative cooling described in the main text. The parameter set which resulted in the most stable Fe sediment source was chosen as the default parameter set for the new model version and the corresponding parameters are given in Tab. S1.3.

4 Tuning results: Five best parameter sets

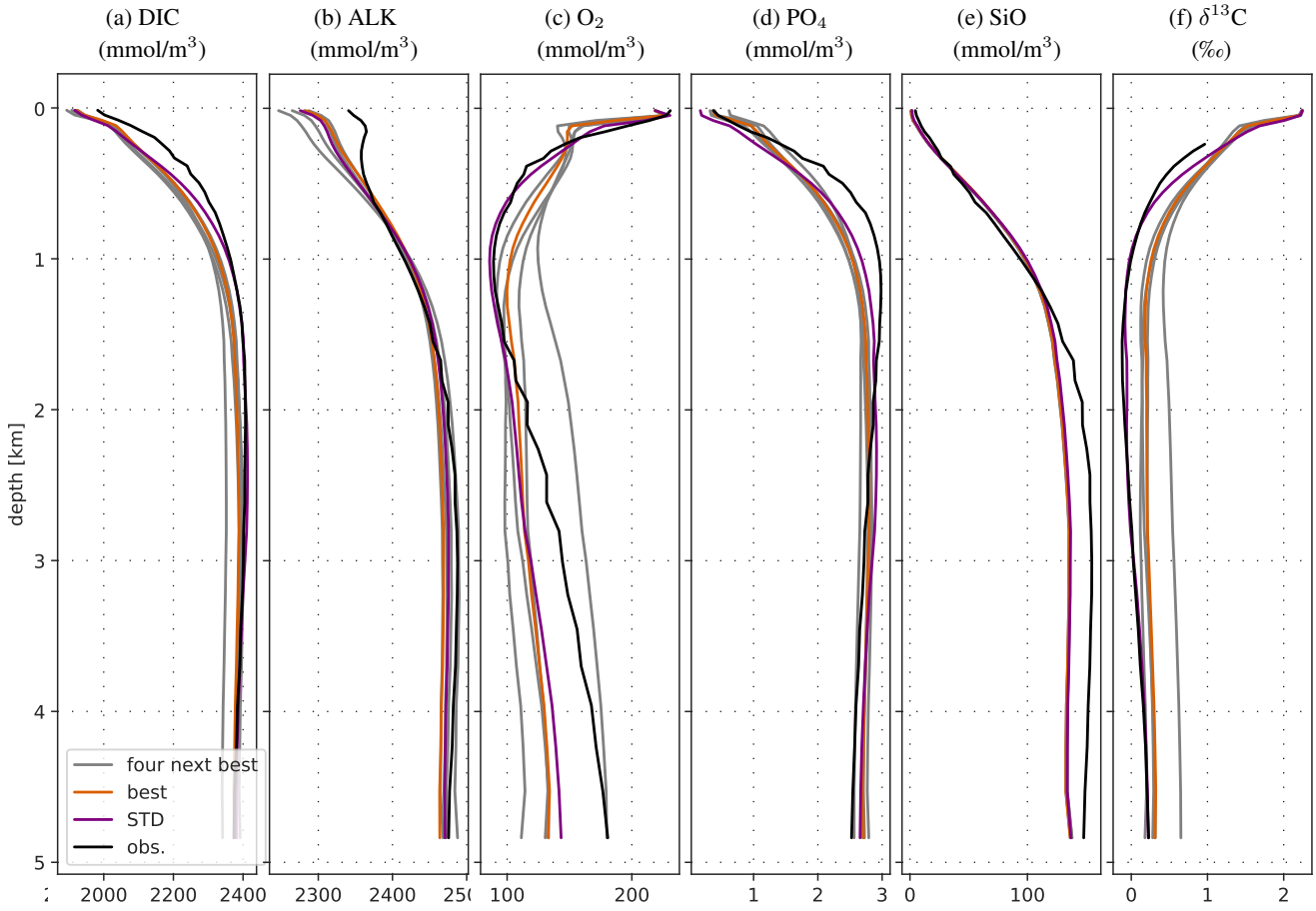

Figure S1.3. Basin-averaged vertical profiles of biochemical species used for the benchmarking of the tuning ensemble for the Pacific. Black are observations, purple is the default Bern3D with Martin curve and simple Fe scheme ('STD') and other colours are the five best tuning ensemble members. The orange line is the new default setting with dynamic particle fluxes and the updated Fe scheme.

The tuned modules improve the overall fit of the simulated biogeochemical fields to observations, and for individual metrics, the vertical profiles and model errors compared to observations are either improved or remained similar compared to the old model version (Fig. S1.3, S2.13, S2.14, S2.15). This is the result of reductions of the model error in various regions, particularly the East Equatorial Pacific and the South Pacific Gyre, while model errors in other areas slightly increased, e.g. in the abyssal Pacific (S2.16, S2.17, S2.18, S2.19, S2.20, S2.21).

Once spun up, when atmospheric CO_2 restoring is relaxed, atmospheric CO_2 drops by 2.4 ppm in the new default version due to re-partitioning between ocean and atmosphere.

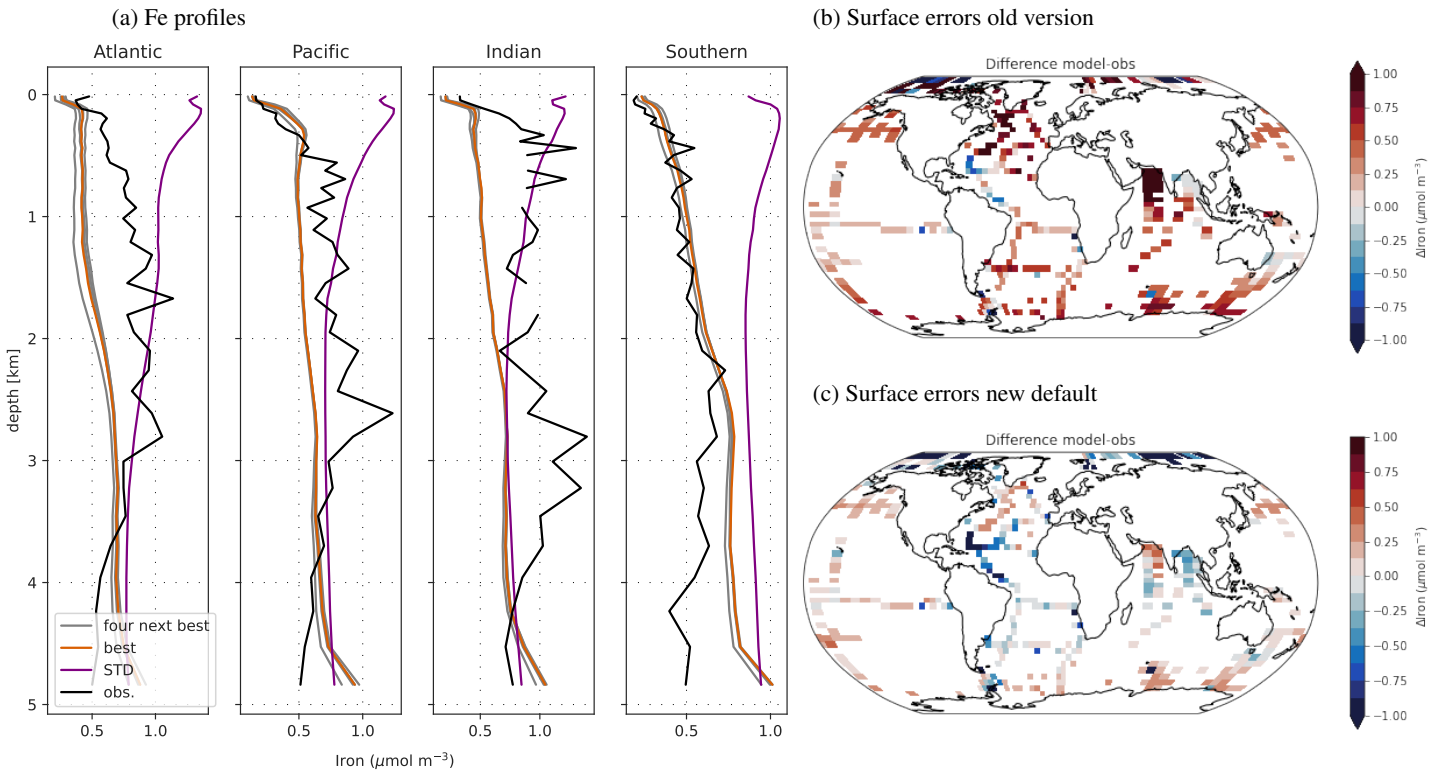

Figure S1.4. Mean error of 3D and surface Fe fields compared to GEOTRACES in the tuning members with the highest overall score and the default Bern3D with Martin curve and simple Fe scheme ('STD').

In particular, Fe in the surface and in the Southern Ocean is more data consistent with the new modules (Fig. S1.4). Somes et al. (2021) found that high sedimentary Fe release (114 Gmol/yr) is required in their model to best reproduce Fe distribution in the ocean. In our model, we cannot maintain such high Fe release fluxes because we do not consider an unlimited sedimentary Fe source but require that the sedimentary Fe release does not exceed sedimentary Fe accumulation with our 'bucket model'. Our sedimentary Fe release is much smaller (5 Gmol/yr), and the second biggest Fe source for the ocean after hydrothermal input (11.4 Gmol/yr) and dissolution from dust (2.8 Gmol/yr).

5 Evaluation of the marine biogeochemical cycle in the pre-industrial steady state

With the new particle flux and iron schemes, the simulated productivity and biogeochemical tracer fields differ in the spatial pattern and environmental sensitivity of key processes compared to the standard model. Primary production rates of POC and carbonate are lower in the Southern Ocean and South Atlantic, while silicate production in the Southern Ocean and Pacific upwelling zone are increased (Fig. S2.22). In the standard model, the Martin curve assumption mostly leads to overestimation of the attenuation rate of organic particles when compared with sediment trap data (Figures S2.9-S2.12). In some locations, the mismatch is reduced with the new scheme but differences in the observed and simulated attenuation profiles remain.

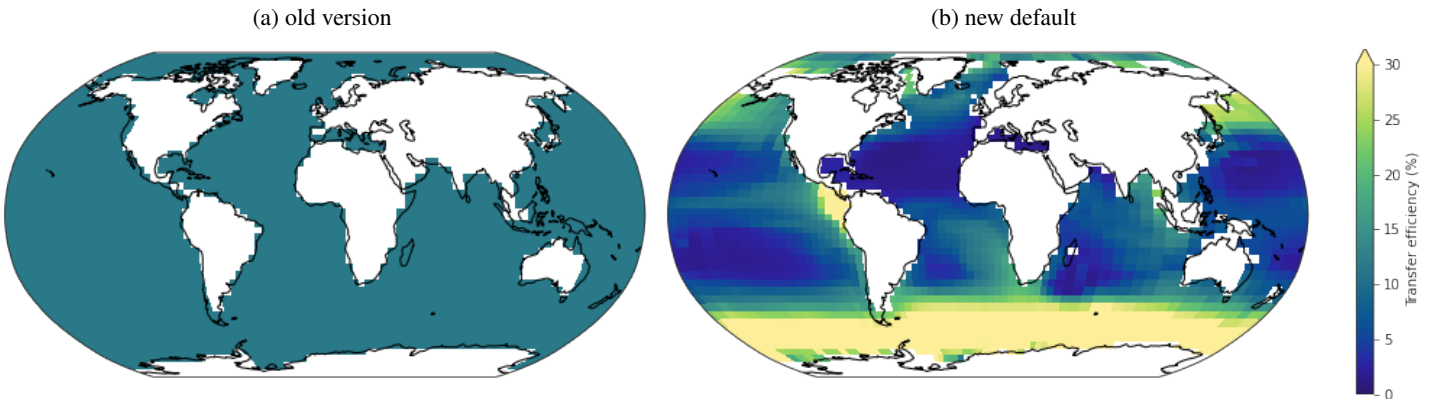

Figure S1.5. Transfer efficiency of particulate organic C into the ocean's interior, evaluated at 1000m depth for the previous (v3.0) and updated (v3.1) versions of Bern3D.

The resulting transfer efficiency, i.e. the fraction of organic particles that reaches depths below 1000 m, is highest in the polar and subpolar oceans and tropical high-productivity zones, related to low temperatures or oxygen. This large-scale pattern matches estimates combining satellite-derived and in-situ observations of production and remineralization in the upper water column (DeVries and Weber, 2017). Regionally and seasonally, transfer efficiency also varies with ecosystem composition and organic matter degradability (Henson et al., 2019). Our model only captures the temperature dependence, but assumes equal degradability globally. Thus, the simulated pattern of transfer efficiency reflects the lower remineralization rates in the polar oceans only. This is short coming would require a more complex primary production scheme and possibly an ecosystem model, which can be the focus of future model development. In their absence, our model setup shows similar transfer efficiency biases as those CMIP6 models which do not capture the spatial pattern of degradability and ecosystem structure (Wilson et al., 2022).

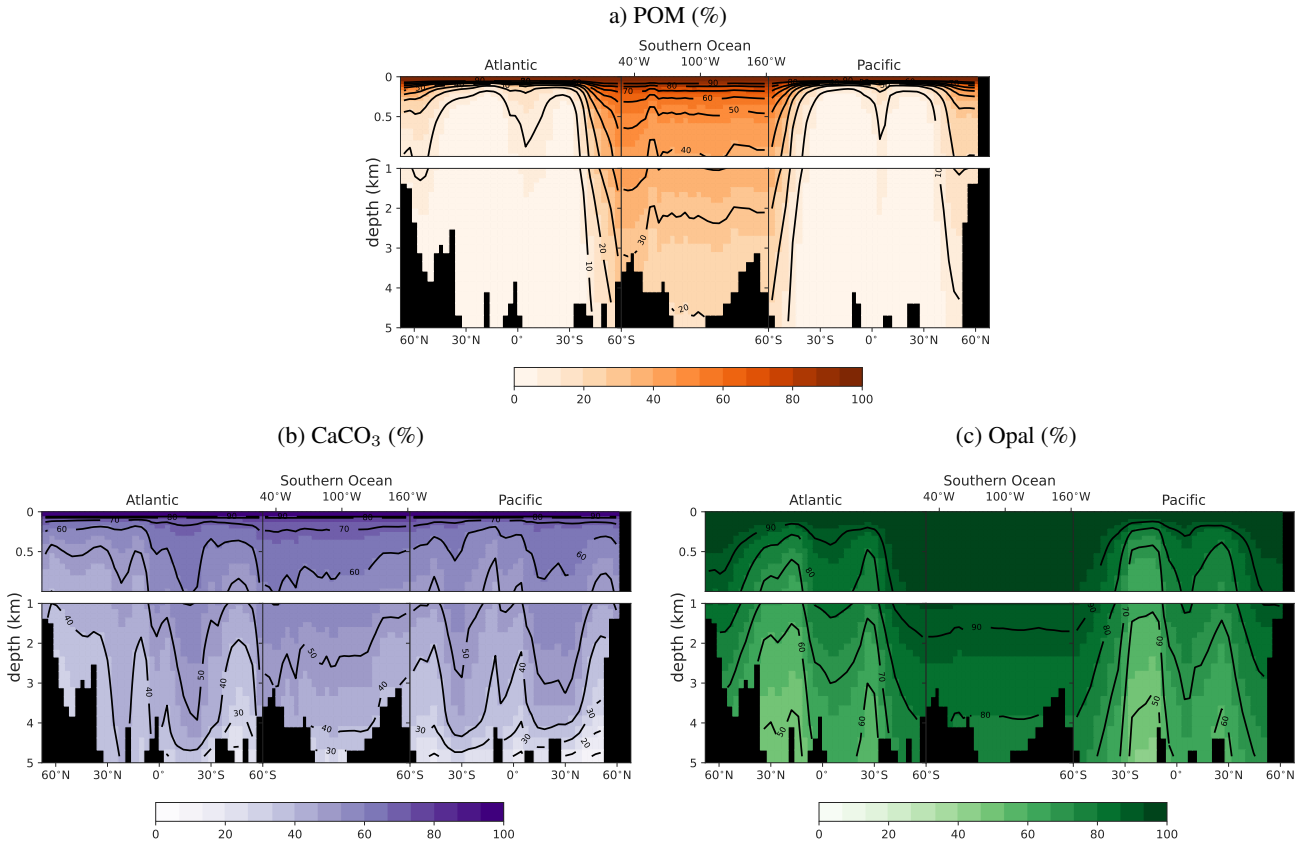

Figure S1.6. Global transects of biogenic particle preservation with depth in the new default Bern3D v3.1.

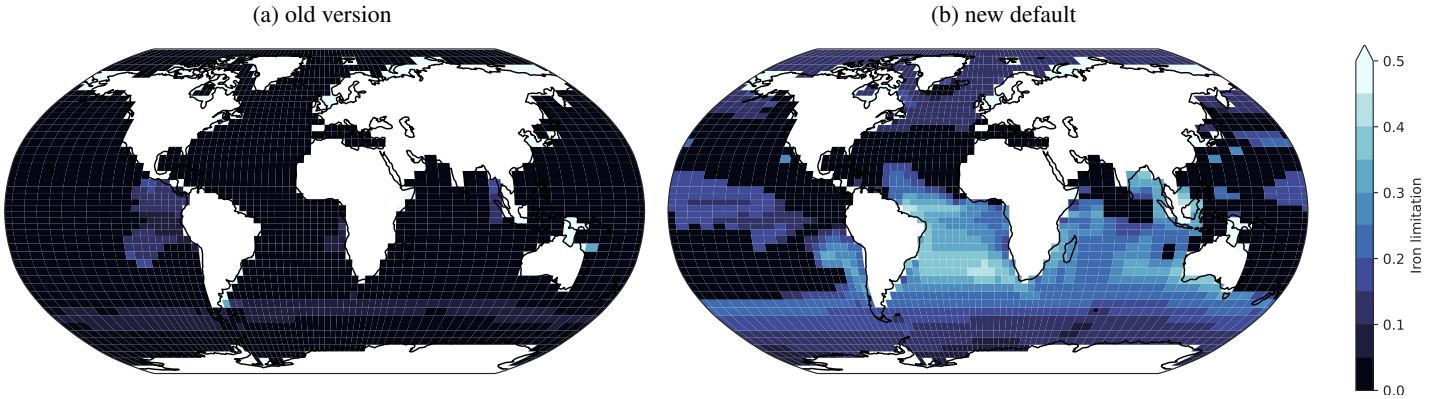

Figure S1.7. Locations and strength of effective Fe limitation for the previous (v3.0) and updated (v3.1) versions of Bern3D.

The altered Fe inputs and scavenging lowered surface Fe concentrations compared to the standard model (Fig. **??**), which increases the Fe-limitation on primary production. With the new schemes, Fe availability is the dominant limitation on pro-

duction in the subpolar Southern Ocean, tropical upwelling zones, North Pacific and the South Atlantic (Fig. S1.7). In the Southern Ocean, North Pacific and upwelling zones, this is consistent with field studies observing increased production after Fe injection (Moore et al., 2013). In the South Atlantic subtropical gyre, field experiments showed nitrogen limitation, which is not simulated in our model but low Fe availability might contribute to low local N_2 fixation rates in the real ocean (Mark Moore et al., 2009). However, the simulated nutrient limitation in the South Atlantic in the new default version is likely somewhat too large, given that it resulted in surface phosphate concentrations that are higher than observed (Fig. S2.13).

6 Evaluation of sedimentary reservoirs

We extended the PI spin-up with the new modules by a 50 kyr-long run including interactive marine sediments to assess the implications of the new particle fluxes on fluxes across the ocean-sediment interface and sedimentary carbon stocks.

Table S1.4. Global carbon cycle metrics.

Metric	Bern3D v3.1
POC export (GtC yr^{-1})	13.55
POC flux 1000m (GtC yr^{-1})	1.44
Export efficiency	0.12
POC deposition (GtC yr^{-1})	0.91
POC burial (GtC yr^{-1})	0.16
POC stock (GtC)	339
$CaCO_3$ export (GtC yr^{-1})	1.0
$CaCO_3$ deposition (GtC yr^{-1})	0.29
$CaCO_3$ burial (GtC yr^{-1})	0.1
$CaCO_3$ stock (GtC)	550
Opal export (Tmol Si yr^{-1})	133.3
Opal deposition (Tmol Si yr^{-1})	79.5
Opal burial (Tmol Si yr^{-1})	3.38
Opal stock (Tmol Si)	15255

The sedimentary $CaCO_3$ stock in the new default version (550 GtC) is considerably lower than the 1000 GtC that were estimated to reside in the top 10 cm of marine sediments by Jeltsch-Thömmes et al. (2019). This is largely the result of too little $CaCO_3$ in sediments in the Equatorial Pacific and South Atlantic (Fig. S1.8). POC contents, in turn are too high, particularly in the Eastern Equatorial Pacific. Similar discrepancies existed in an older Bern3d model version and suggests that the sediment module needs to be re-tuned to achieve more data-consistent sediment compositions, as previously done in Jeltsch-Thömmes et al. (2019) for the previous Fe and particle schemes.

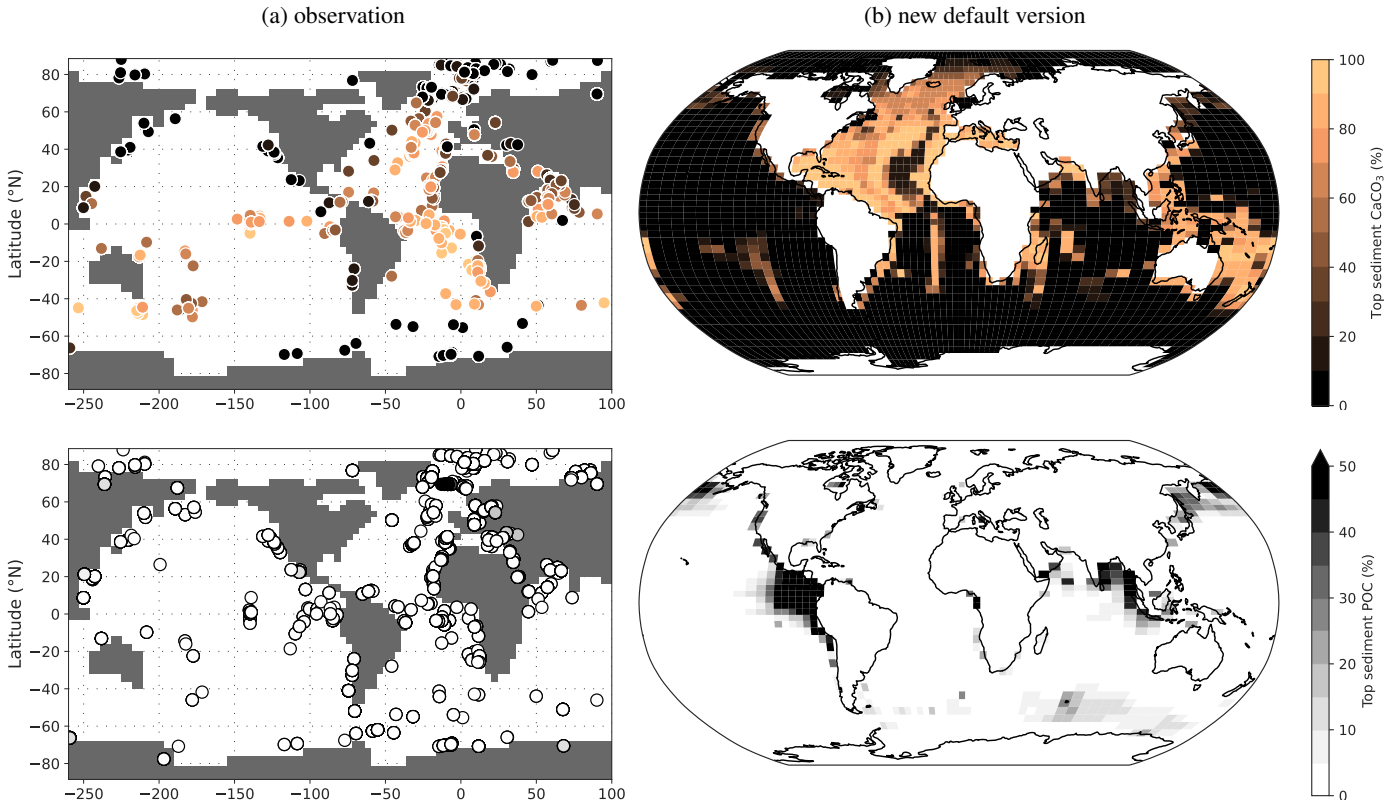

Figure S1.8. Weight-percentage of $CaCO_3$ and POC in surface sediments from observations (Cartapanis et al., 2016, 2018) and as simulated by the new default setup with dynamic particle fluxes and updated Fe cycling with interactive sediments (average over top 10 cm).

References

Aumont, O., Éthé, C., Tagliabue, A., Bopp, L., and Gehlen, M. (2015). Pisces-v2: an ocean biogeochemical model for carbon and ecosystem studies. *Geoscientific Model Development Discussions*, 8(2):1375–1509.

Battaglia, G. and Joos, F. (2018). Marine n_2o emissions from nitrification and denitrification constrained by modern observations and projected in multimillennial global warming simulations. *Global Biogeochemical Cycles*, 32(1):92–121.

Cartapanis, O., Bianchi, D., Jaccard, S. L., and Galbraith, E. D. (2016). Global pulses of organic carbon burial in deep-sea sediments during glacial maxima. *NAT COMMUN*, 7(1):10796.

Cartapanis, O., Galbraith, E. D., Bianchi, D., and Jaccard, S. L. (2018). Carbon burial in deep-sea sediment and implications for oceanic inventories of carbon and alkalinity over the last glacial cycle. *CLIM PAST*, 14(11):1819–1850.

Cliff, E., Khatiwala, S., and Schmittner, A. (2021). Glacial deep ocean deoxygenation driven by biologically mediated air–sea disequilibrium. *Nature Geoscience*, 14(1):43–50.

Dale, A. W., Nickelsen, L., Scholz, F., Hensen, C., Oschlies, A., and Wallmann, K. (2015). A revised global estimate of dissolved iron fluxes from marine sediments. *Global Biogeochemical Cycles*, 29(5):691–707.

DeVries, T. and Weber, T. (2017). The export and fate of organic matter in the ocean: New constraints from combining satellite and oceanographic tracer observations. *Global Biogeochemical Cycles*, 31(3):535–555.

Dinauer, A., Laufkötter, C., Doney, S. C., and Joos, F. (2022). What controls the large-scale efficiency of carbon transfer through the ocean's mesopelagic zone? insights from a new, mechanistic model (mspacmam). *Global biogeochemical cycles*, 36(10):e2021GB007131.

Floegel, S., Wallmann, K., Poulsen, C., Zhou, J., Oschlies, A., Voigt, S., and Kuhnt, W. (2011). Simulating the biogeochemical effects of volcanic co2 degassing on the oxygen-state of the deep ocean during the cenomanian/turonian anoxic event (oae2). *Earth and Planetary Science Letters*, 305(3-4):371–384.

Henson, S., Le Moigne, F., and Giering, S. (2019). Drivers of carbon export efficiency in the global ocean. *Global biogeochemical cycles*, 33(7):891–903.

Jeltsch-Thömmes, A., Battaglia, G., Cartapanis, O., Jaccard, S. L., and Joos, F. (2019). Low terrestrial carbon storage at the last glacial maximum: constraints from multi-proxy data. *Climate of the Past*, 15(2):849–879.

Kwiatkowski, L., Aumont, O., Bopp, L., and Ciais, P. (2018). The impact of variable phytoplankton stoichiometry on projections of primary production, food quality, and carbon uptake in the global ocean. *Global Biogeochemical Cycles*, 32(4):516–528.

Liang, H., Lunstrum, A. M., Dong, S., Berelson, W. M., and John, S. G. (2023). Constraining $caco_3$ export and dissolution with an ocean alkalinity inverse model. *Global Biogeochemical Cycles*, 37(2):e2022GB007535.

Mahowald, N. M., Muhs, D. R., Levis, S., Rasch, P. J., Yoshioka, M., Zender, C. S., and Luo, C. (2006). Change in atmospheric mineral aerosols in response to climate: Last glacial period, preindustrial, modern, and doubled carbon dioxide climates. *Journal of Geophysical Research: Atmospheres*, 111(D10).

Mark Moore, C., Mills, M. M., Achterberg, E. P., Geider, R. J., LaRoche, J., Lucas, M. I., McDonagh, E. L., Pan, X., Poulton, A. J., Rijkenberg, M. J., et al. (2009). Large-scale distribution of atlantic nitrogen fixation controlled by iron availability. *Nature Geoscience*, 2(12):867–871.

Moore, C., Mills, M., Arrigo, K., Berman-Frank, I., Bopp, L., Boyd, P., Galbraith, E., Geider, R., Guieu, C., Jaccard, S., et al. (2013). Processes and patterns of oceanic nutrient limitation. *Nature geoscience*, 6(9):701–710.

Moore, J. K. and Braucher, O. (2008). Sedimentary and mineral dust sources of dissolved iron to the world ocean. *Biogeosciences*, 5(3):631–656.

Nickelsen, L., Keller, D., and Oschlies, A. (2015). A dynamic marine iron cycle module coupled to the University of Victoria Earth System Model: the Kiel Marine Biogeochemical Model 2 (KMBM2) for UVic.

Niemeyer, D., Kemena, T. P., Meissner, K. J., and Oschlies, A. (2017). A model study of warming-induced phosphorus–oxygen feedbacks in open-ocean oxygen minimum zones on millennial timescales. *Earth System Dynamics*, 8(2):357–367.

Parekh, P., Follows, M. J., and Boyle, E. (2004). Modeling the global ocean iron cycle. *Global biogeochemical cycles*, 18(1).

Sharqawy, M. H., Lienhard, J. H., and Zubair, S. M. (2010). Thermophysical properties of seawater: a review of existing correlations and data. *Desalination and water treatment*, 16(1-3):354–380.

Somes, C. J., Dale, A. W., Wallmann, K., Scholz, F., Yao, W., Oschlies, A., Muglia, J., Schmittner, A., and Achterberg, E. P. (2021). Constraining Global Marine Iron Sources and Ligand-Mediated Scavenging Fluxes With GEOTRACES Dissolved Iron Measurements in an Ocean Biogeochemical Model. *Global Biogeochemical Cycles*, 35(8):e2021GB006948.

Tagliabue, A., Buck, K. N., Sofen, L. E., Twining, B. S., Aumont, O., Boyd, P. W., Caprara, S., Homoky, W. B., Johnson, R., König, D., et al. (2023). Authigenic mineral phases as a driver of the upper-ocean iron cycle. *Nature*, 620(7972):104–109.

Völker, C. and Tagliabue, A. (2015). Modeling organic iron-binding ligands in a three-dimensional biogeochemical ocean model. *Marine Chemistry*, 173:67–77.

Wilson, J. D., Andrews, O., Katavouta, A., de Melo Viríssimo, F., Death, R. M., Adloff, M., Baker, C. A., Blackledge, B., Goldsworth, F. W., Kennedy-Asser, A. T., et al. (2022). The biological carbon pump in cmip6 models: 21st century trends and uncertainties. *Proceedings of the National Academy of Sciences*, 119(29):e2204369119.

SI Figures

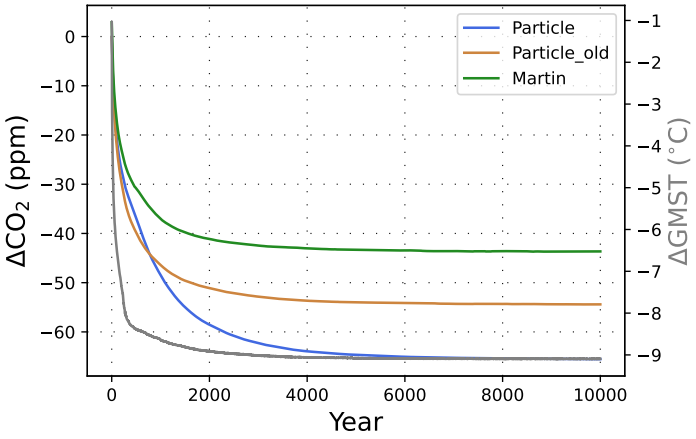

Figure S2.1. Changes in atmospheric CO_2 (colored lines) and global mean surface air temperature (GMST, grey line) in response to the applied negative radiative forcing with the three model set-ups.

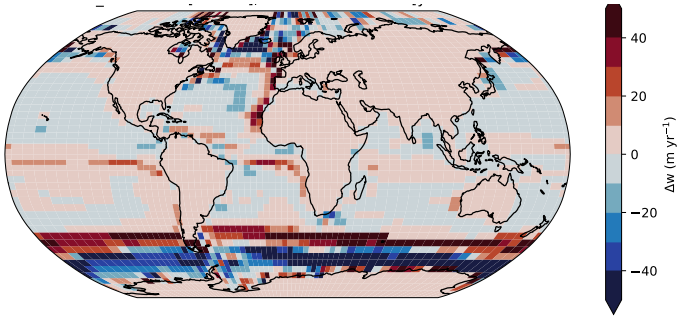

Figure S2.2. Changes of annual mean vertical velocity near the sea surface in response to cooling and evaluated at steady state.

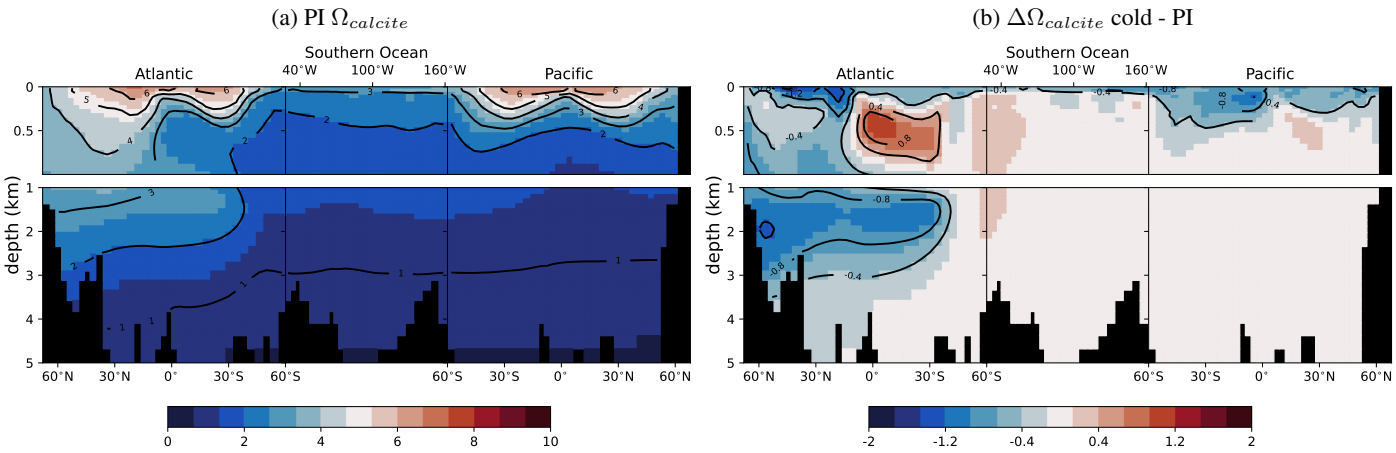

Figure S2.3. Calcite saturation state in the *Martin* PI steady state (a) and the saturation state changes caused by the applied cooling (b).

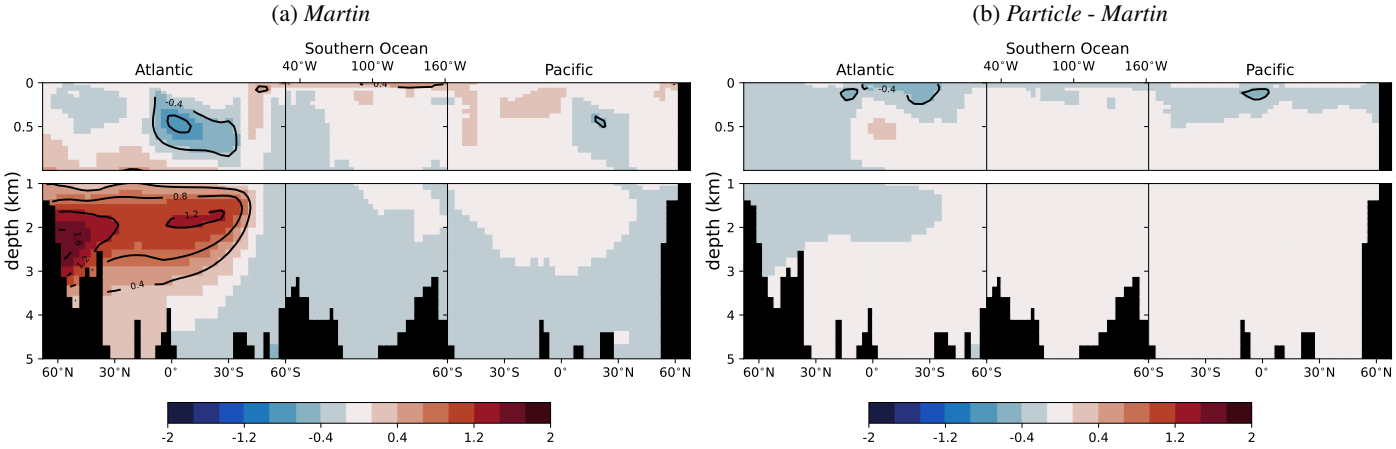

Figure S2.4. PO_4 concentration changes (mmol/m^3) due to cooling in the *Martin* simulations (a = $Martin_{cold}$ - $Martin_{PI}$) and the differences in the *Particle* simulations ($Particle_{cold}$ minus $Particle_{PI}$ - a).

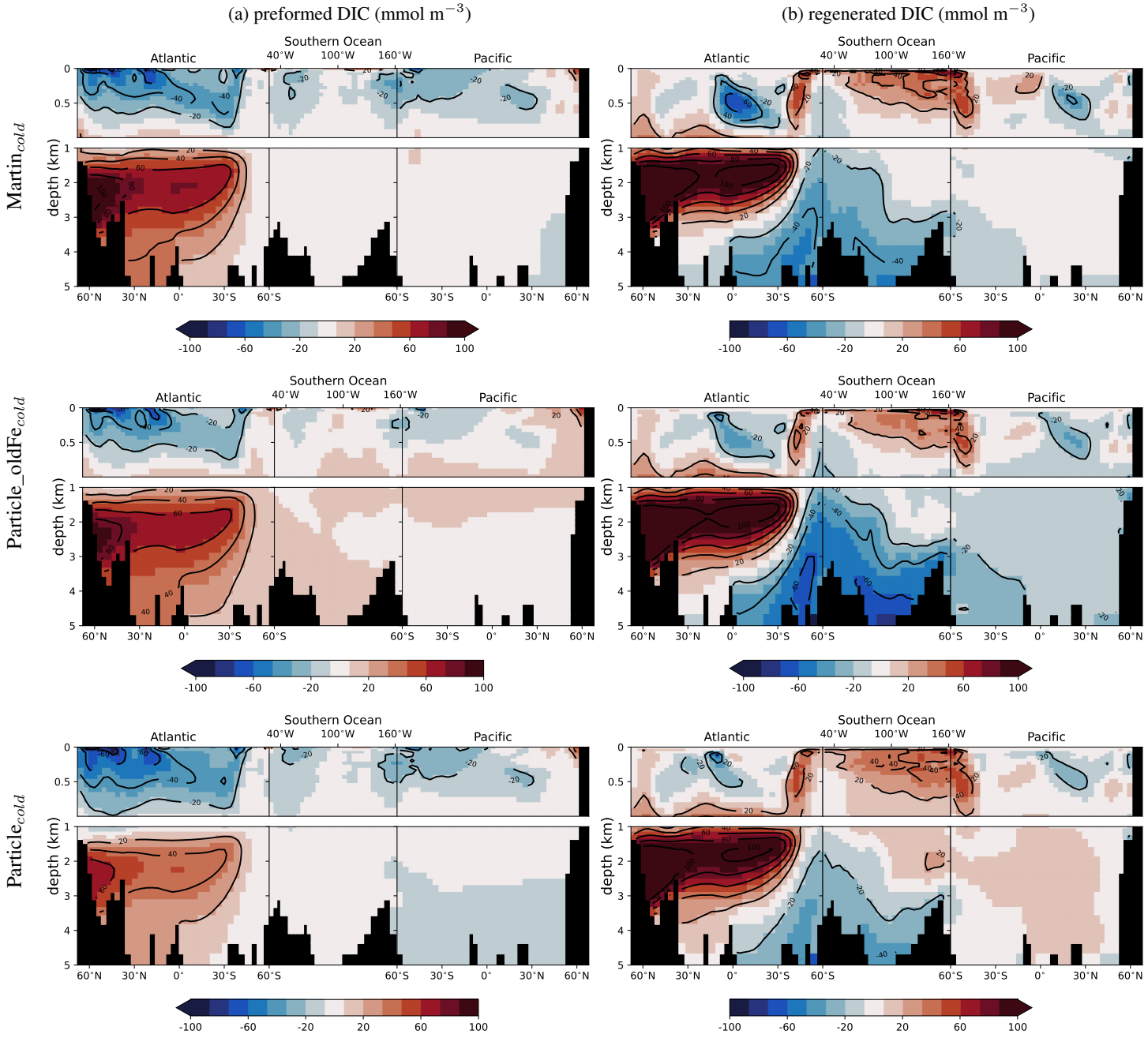

Figure S2.5. Changes of preformed and regenerated concentrations due to cooling in our simulations with Martin curve, dynamic particles and simple Fe scheme, and dynamic particles and complex Fe scheme.

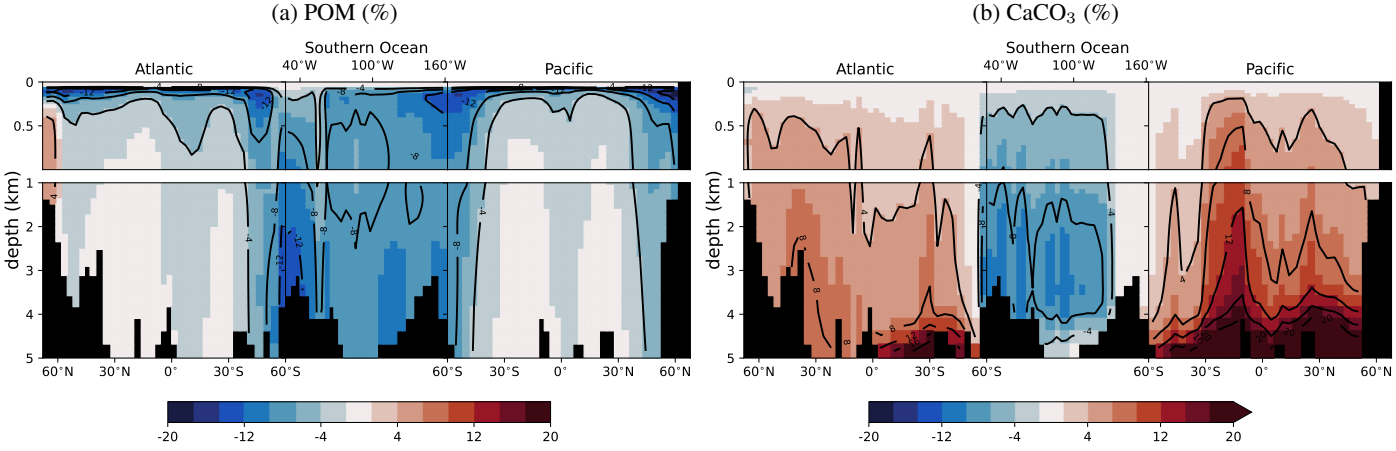

Figure S2.6. Changes in transfer efficiency (absolute % points) due to warming with the dynamic particle scheme (simulation Particle$_{cold}$ minus Particle$_{PI}$). Transfer efficiency at a given depth is defined as the percentage of export flux at 100 m that reaches that depth, shown are changes in absolute percentage points.

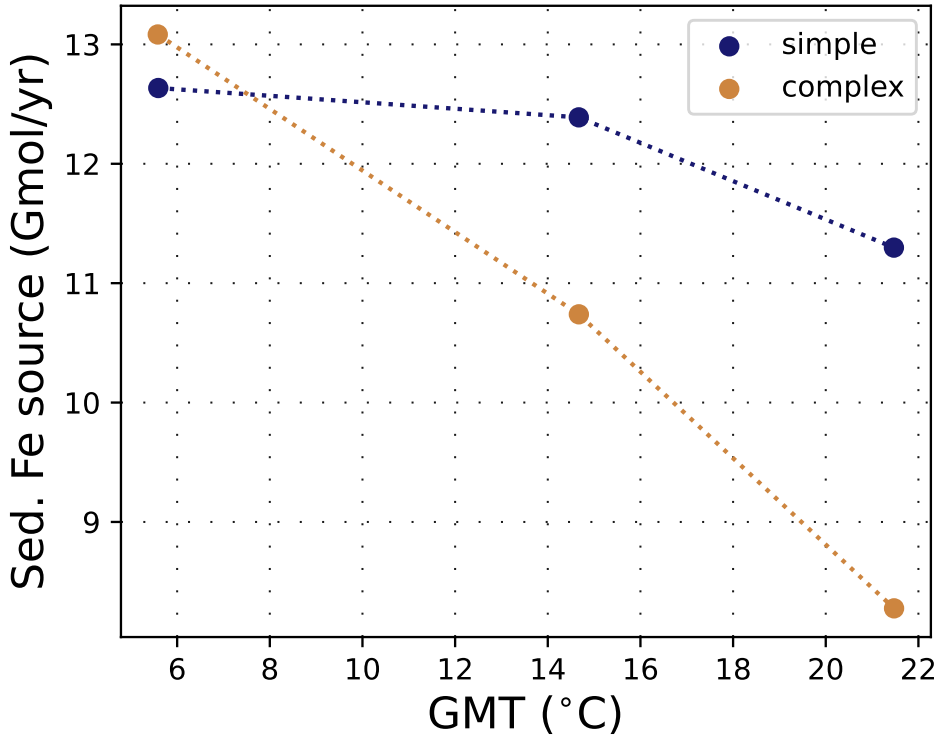

Figure S2.7. Simulated strength of the global sedimentary Fe source in simulations of different climate states, once assuming only a dependence on the settling POM flux (Dale et al., 2015) in the calculation of sedimentary oxydation rates ('simple') and once calculating it from sedimentary organic matter content and pore water conditions ('complex').

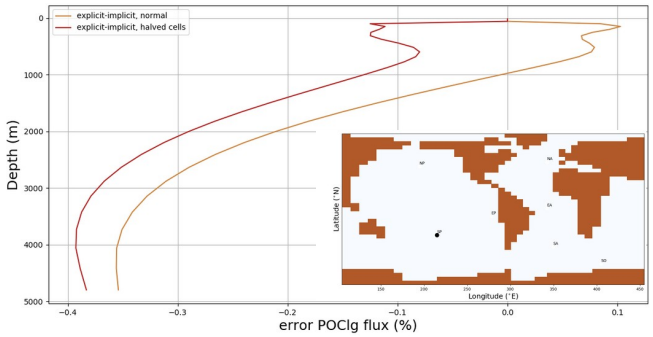
explicit-implicit, normal
explicit-implicit, halved cells
Depth (m)
error POClg flux (%)
Latitude (° N)
Longitude (° E)

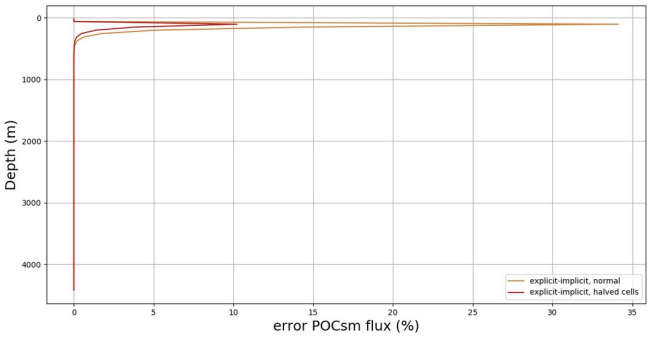
explicit-implicit, normal
explicit-implicit, halved cells
Depth (m)
error POCsm flux (%)

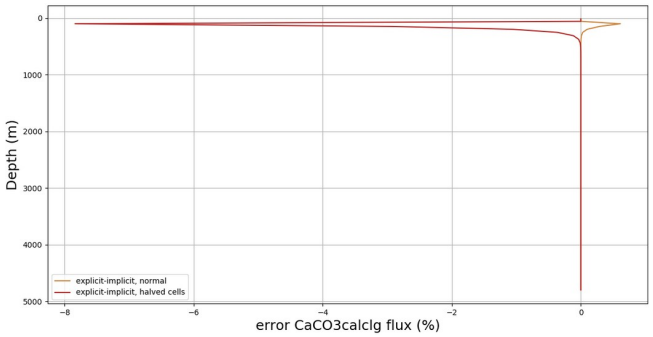
explicit-implicit, normal
explicit-implicit, halved cells
Depth (m)
error CaCO3calclg flux (%)

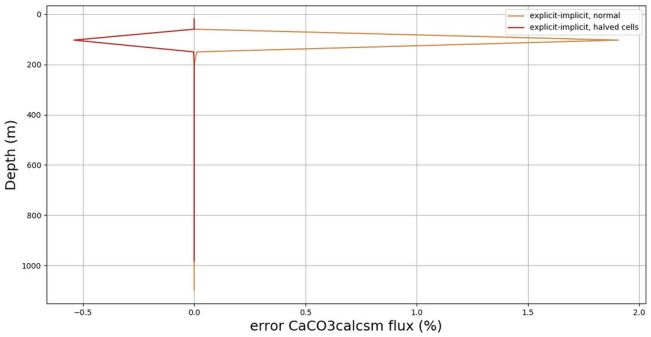
explicit-implicit, normal
explicit-implicit, halved cells
Depth (m)
error CaCO3calcsm flux (%)

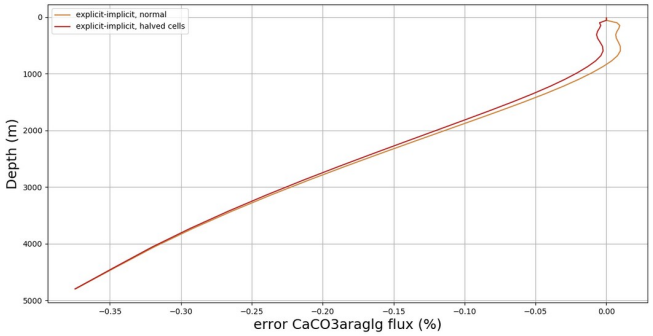
explicit-implicit, normal
explicit-implicit, halved cells
Depth (m)
error CaCO3araglg flux (%)

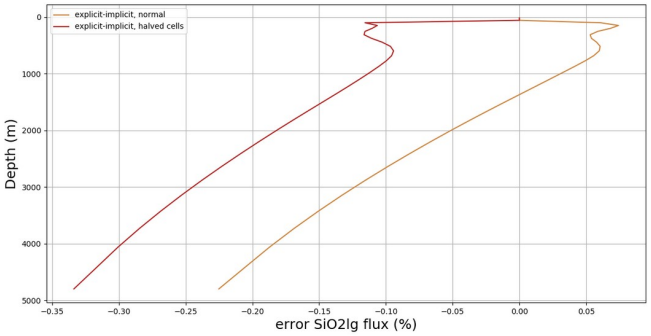
explicit-implicit, normal
explicit-implicit, halved cells
Depth (m)
error SiO2lg flux (%)

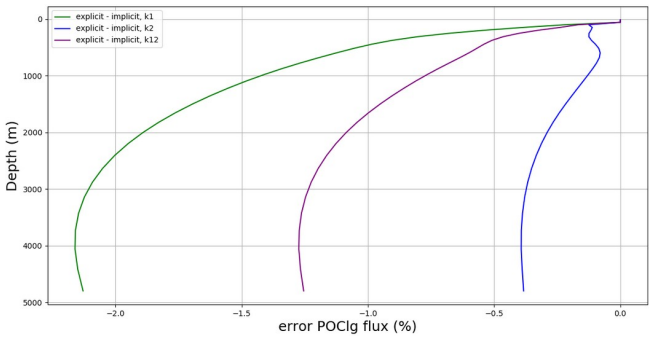
explicit - implicit, k1
explicit - implicit, k2
explicit - implicit, k12
Depth (m)
error POClg flux (%)

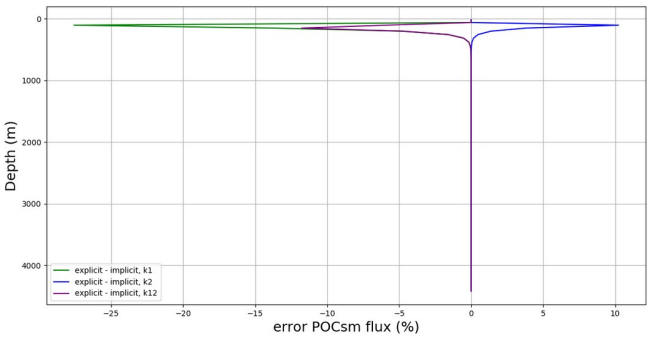
explicit - implicit, k1
explicit - implicit, k2
explicit - implicit, k12
Depth (m)
error POCsm flux (%)

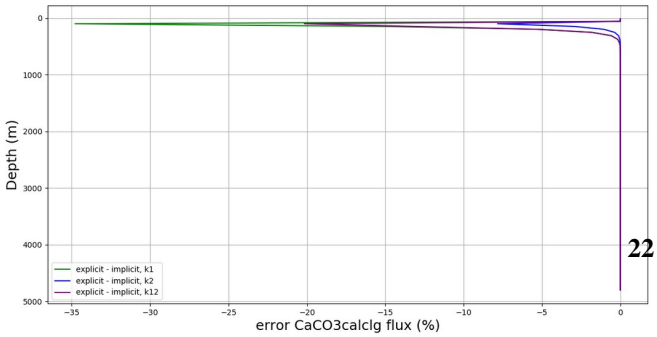
explicit - implicit, k1
explicit - implicit, k2
explicit - implicit, k12
Depth (m)
error CaCO3calclg flux (%)

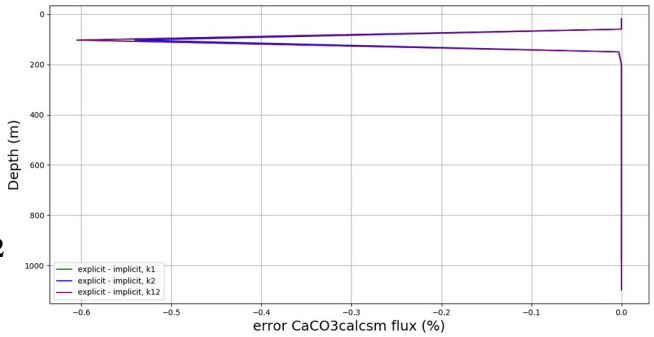
explicit - implicit, k1
explicit - implicit, k2
explicit - implicit, k12
Depth (m)
error CaCO3calcsm flux (%)

36.5°N 122.5°W

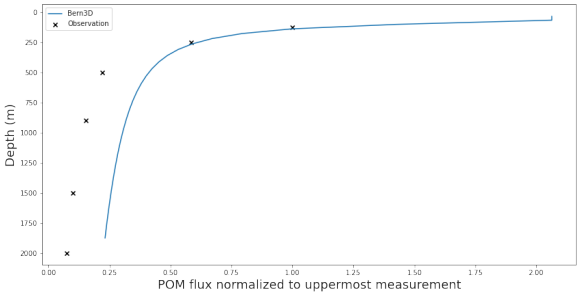

35.5°N 128.5°W

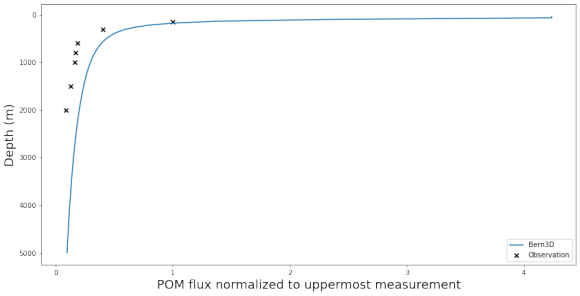

33.5°N 139.5°W

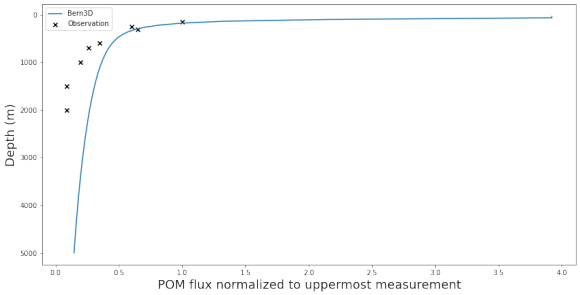

28.5°N 154.5°W

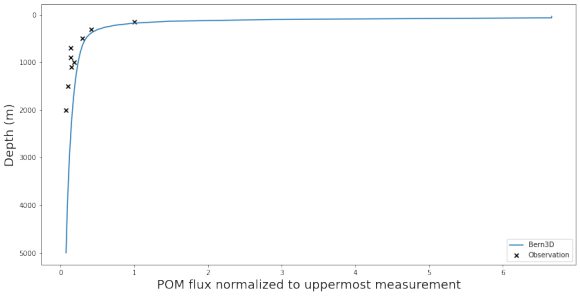

47.5°N 160.5°E

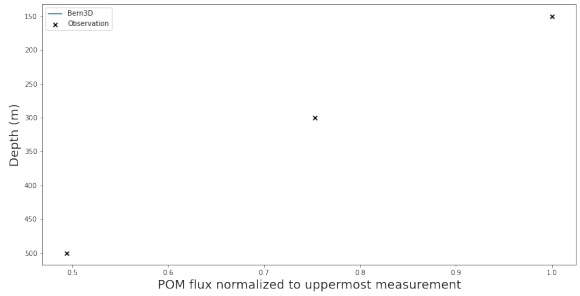

48.5°N 16.5°W

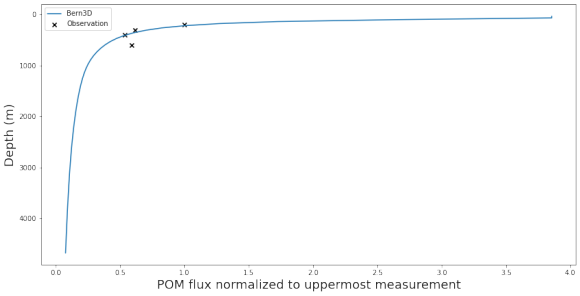

Figure S2.9. Simulated particle fluxes and sediment trap data relative to the shallowest depth for which data is available at each location.

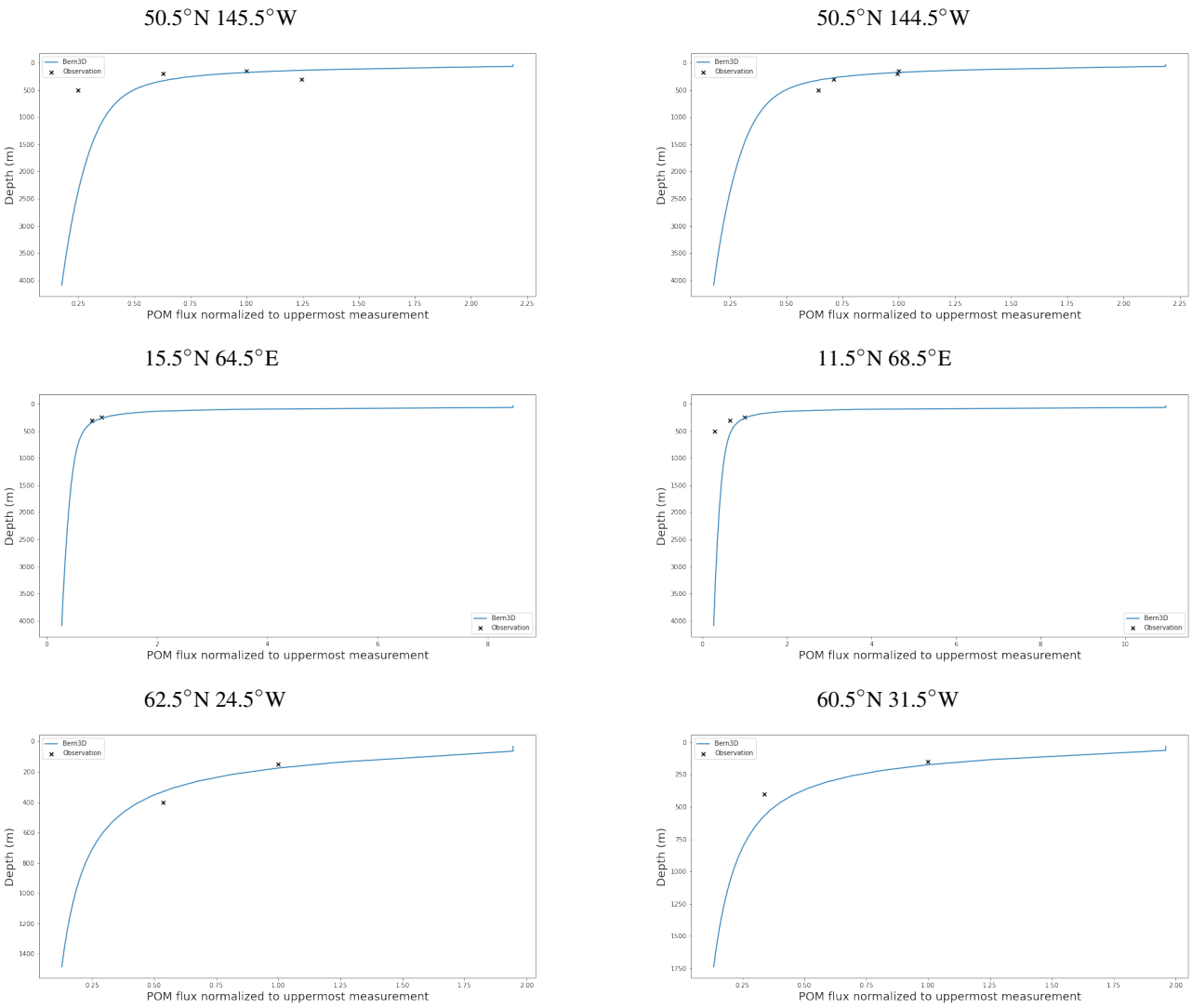

Figure S2.10. Simulated particle fluxes and sediment trap data relative to the shallowest depth for which data is available at each location.

18.5°N 107.5°W

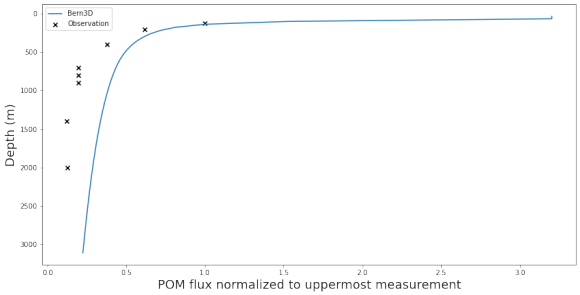

15.5°N 107.5°E

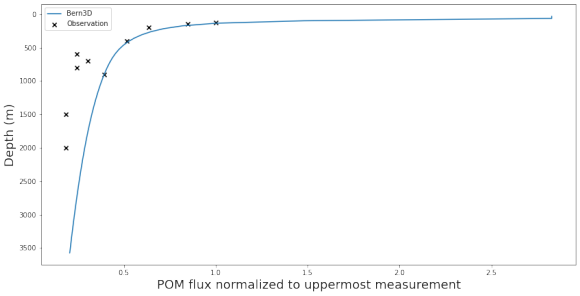

22.5°N 157.5°W

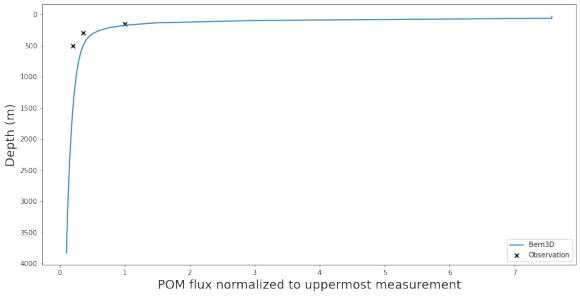

31.5°N 64.5°W

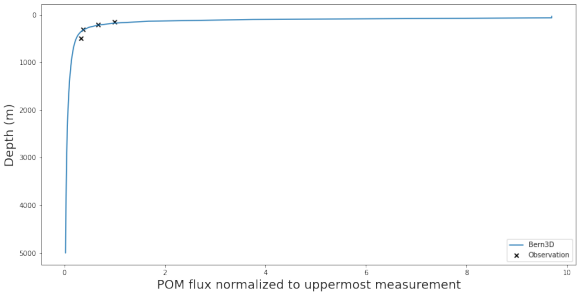

22.5°N 106.5°W

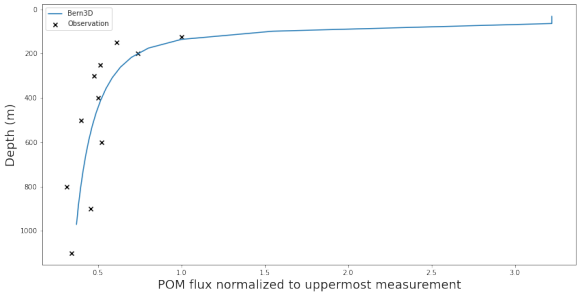

26.5°N 31.5°W

Figure S2.11. Simulated particle fluxes and sediment trap data relative to the shallowest depth for which data is available at each location.

13.5°N 91.5°W

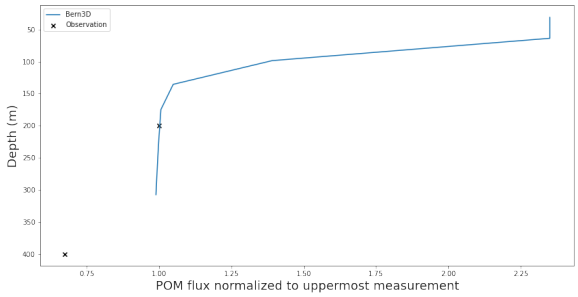

10.5°N 20.5°W

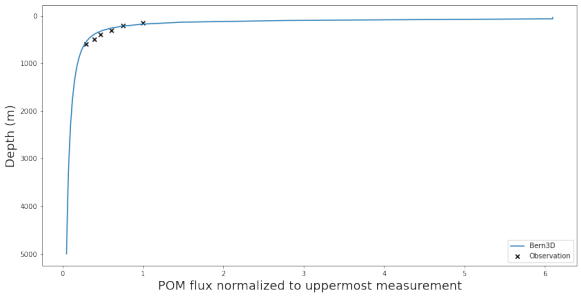

14.5°N 129.5°W

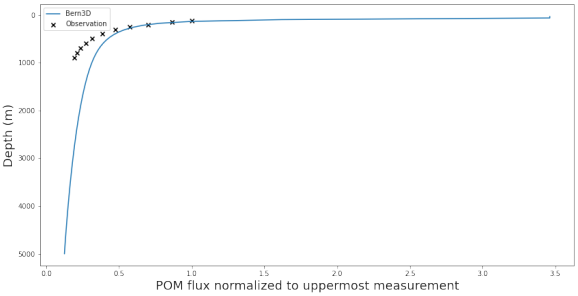

15.5°N 75.5°W

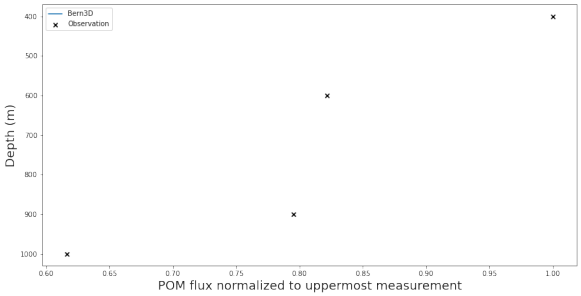

Figure S2.12. Simulated particle fluxes and sediment trap data relative to the shallowest depth for which data is available at each location.

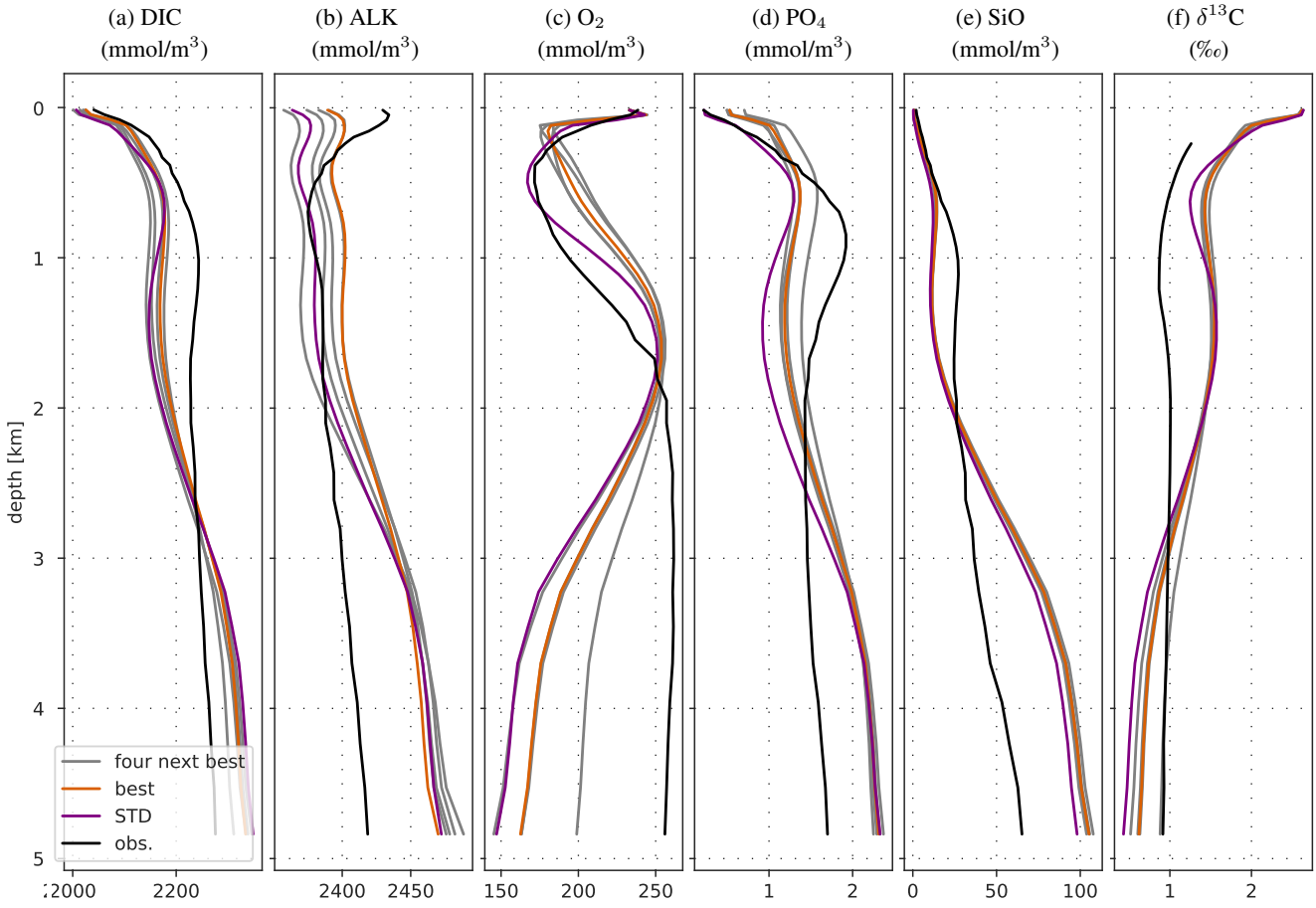

Figure S2.13. Basin-averaged vertical profiles of biochemical species used for the benchmarking of the tuning ensemble for the Atlantic. Black are observations, purple is the previous Bern3D version and the other colors are the best tuning ensemble members.

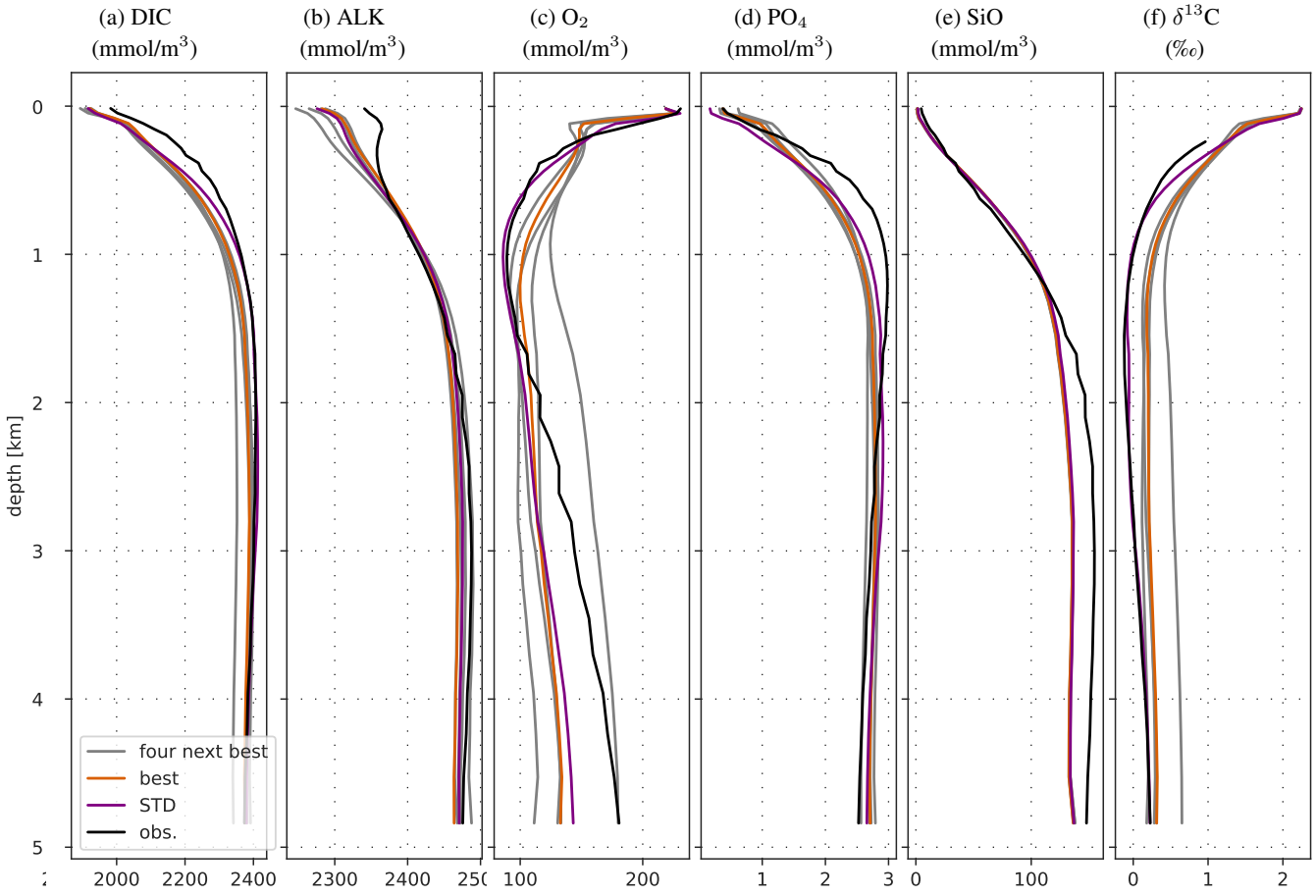

Figure S2.14. Basin-averaged vertical profiles of biochemical species used for the benchmarking of the tuning ensemble for the Indian Ocean. Black are observations, purple is the previous Bern3D version and the other colors are the best tuning ensemble members.

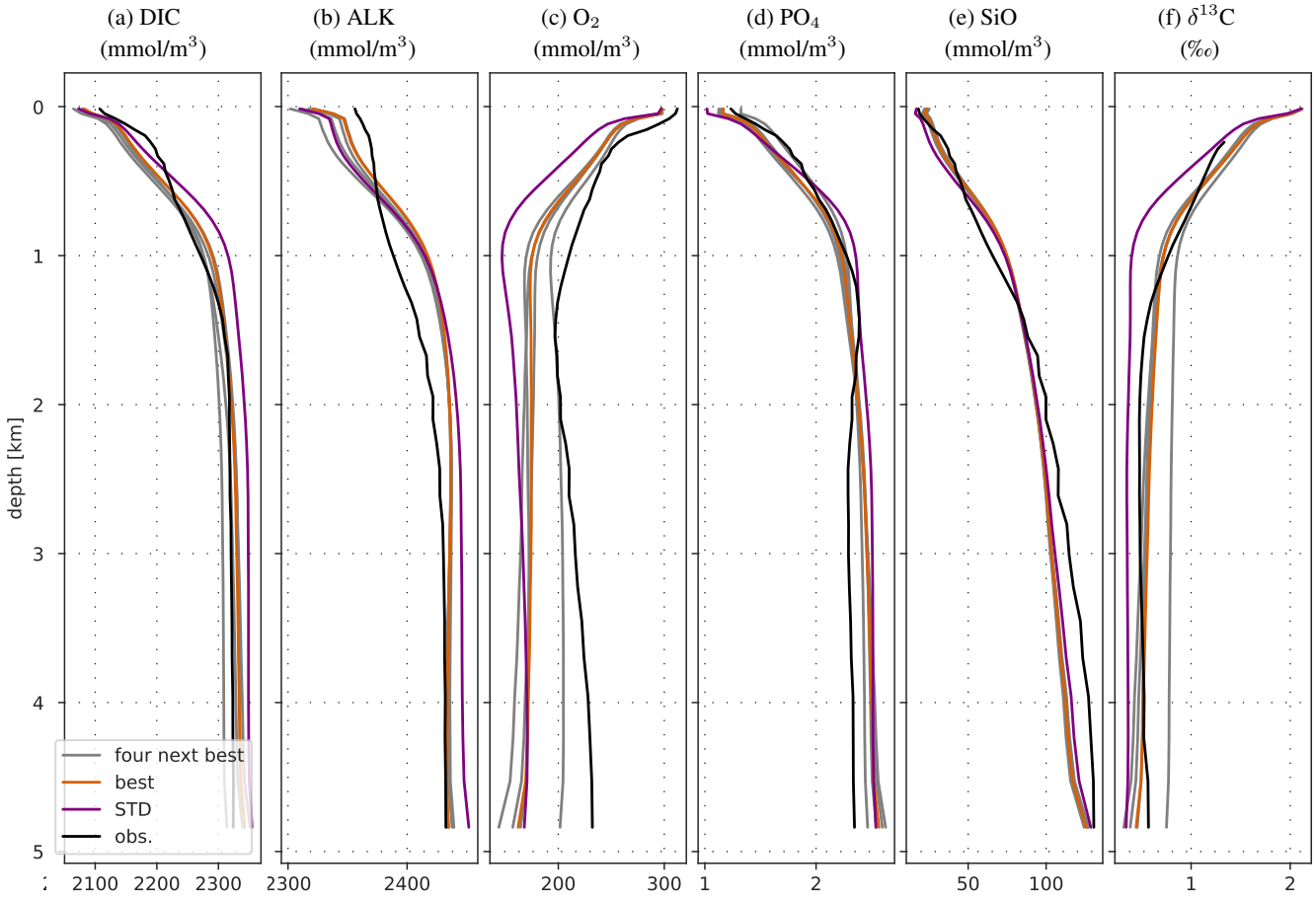

Figure S2.15. Basin-averaged vertical profiles of biochemical species used for the benchmarking of the tuning ensemble for the Southern Ocean. Black are observations, purple is the previous Bern3D version and the other colors are the best tuning ensemble members.

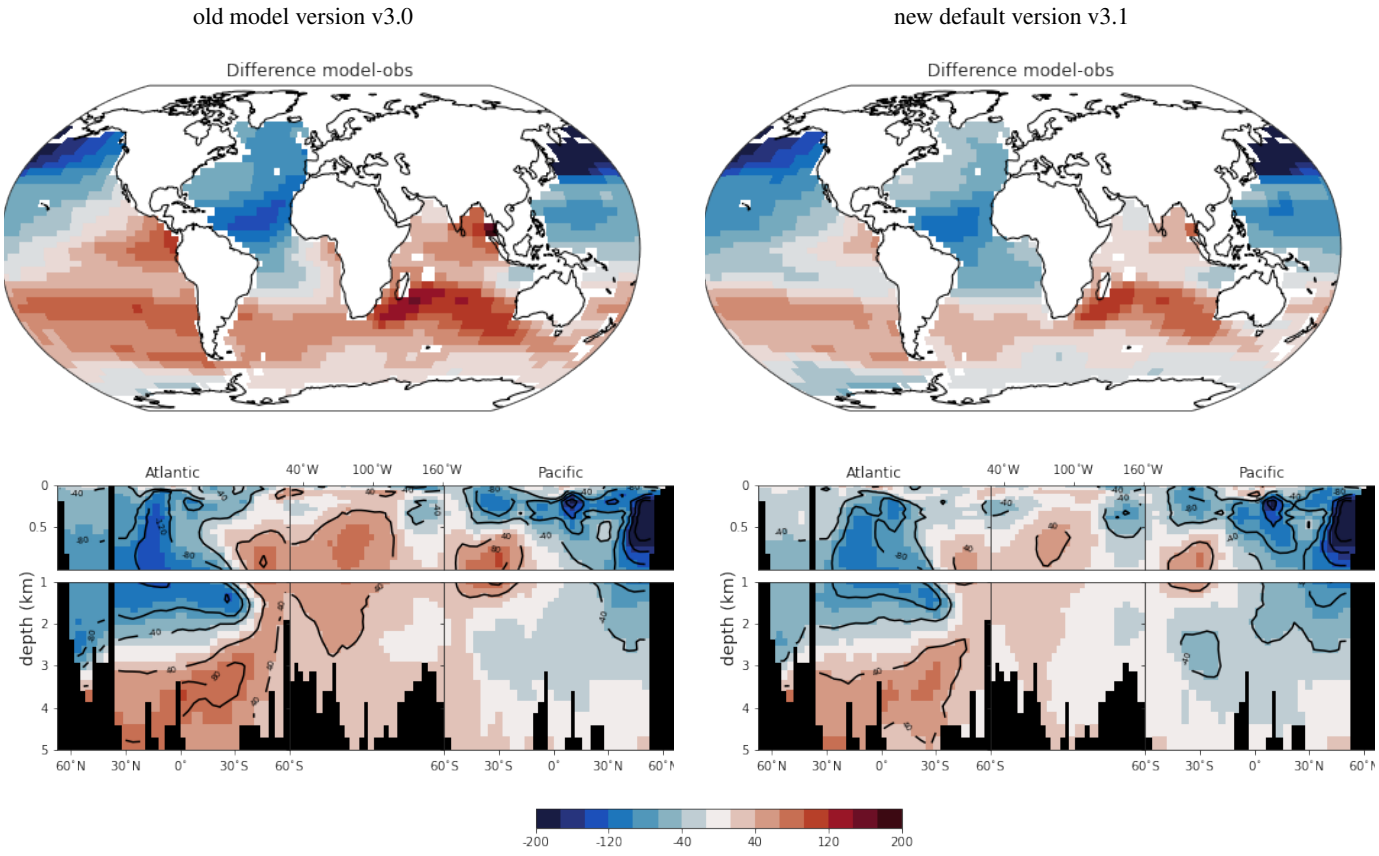

Figure S2.16. Model error of DIC concentrations (mmol/m^3) at 750 m depth and in a transect through three ocean basins in the old and new default model versions.

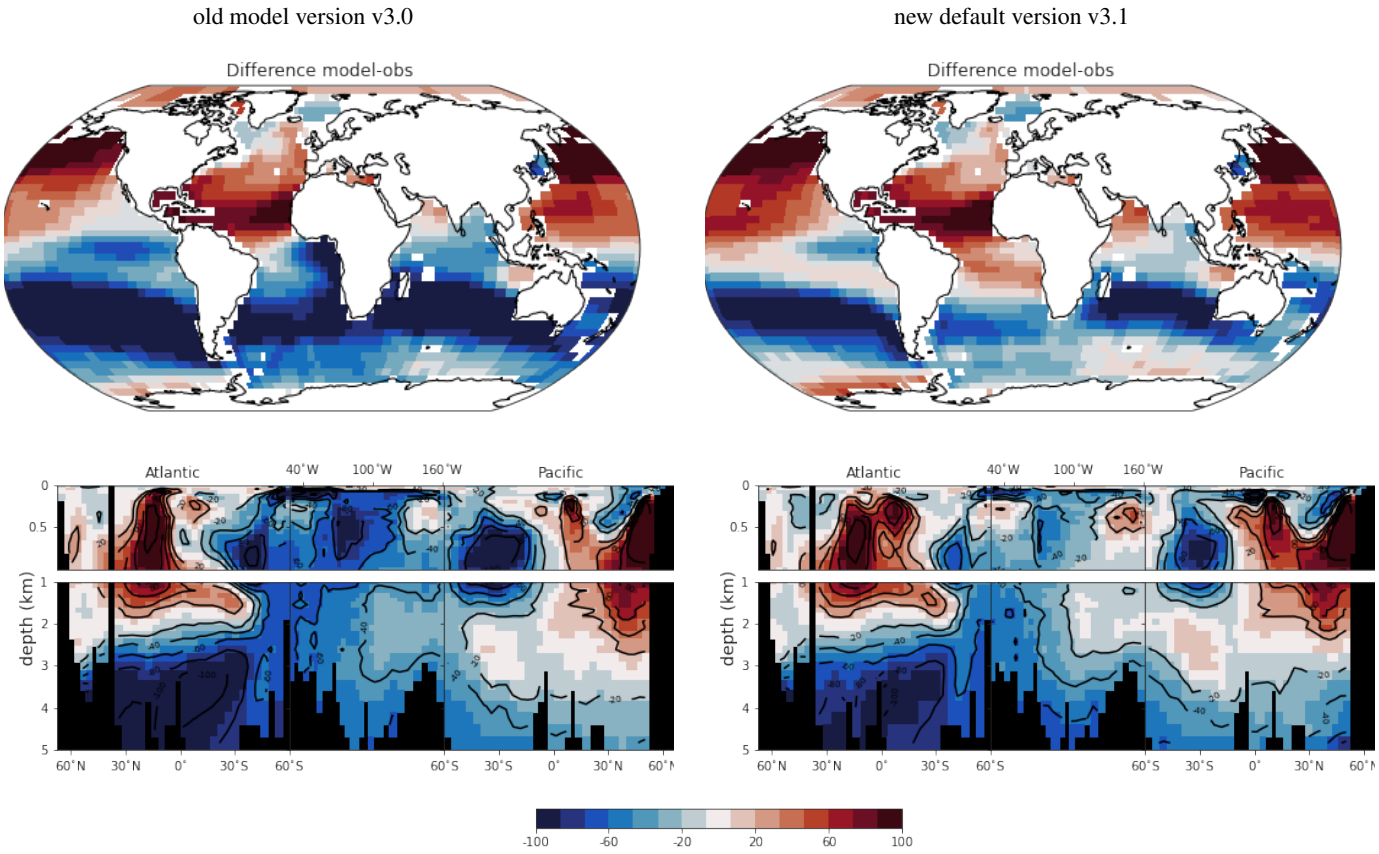

Figure S2.17. Model error of O_2 concentrations (mmol/m^3) at 750 m depth and in a transect through three ocean basins in the old and new default model versions.

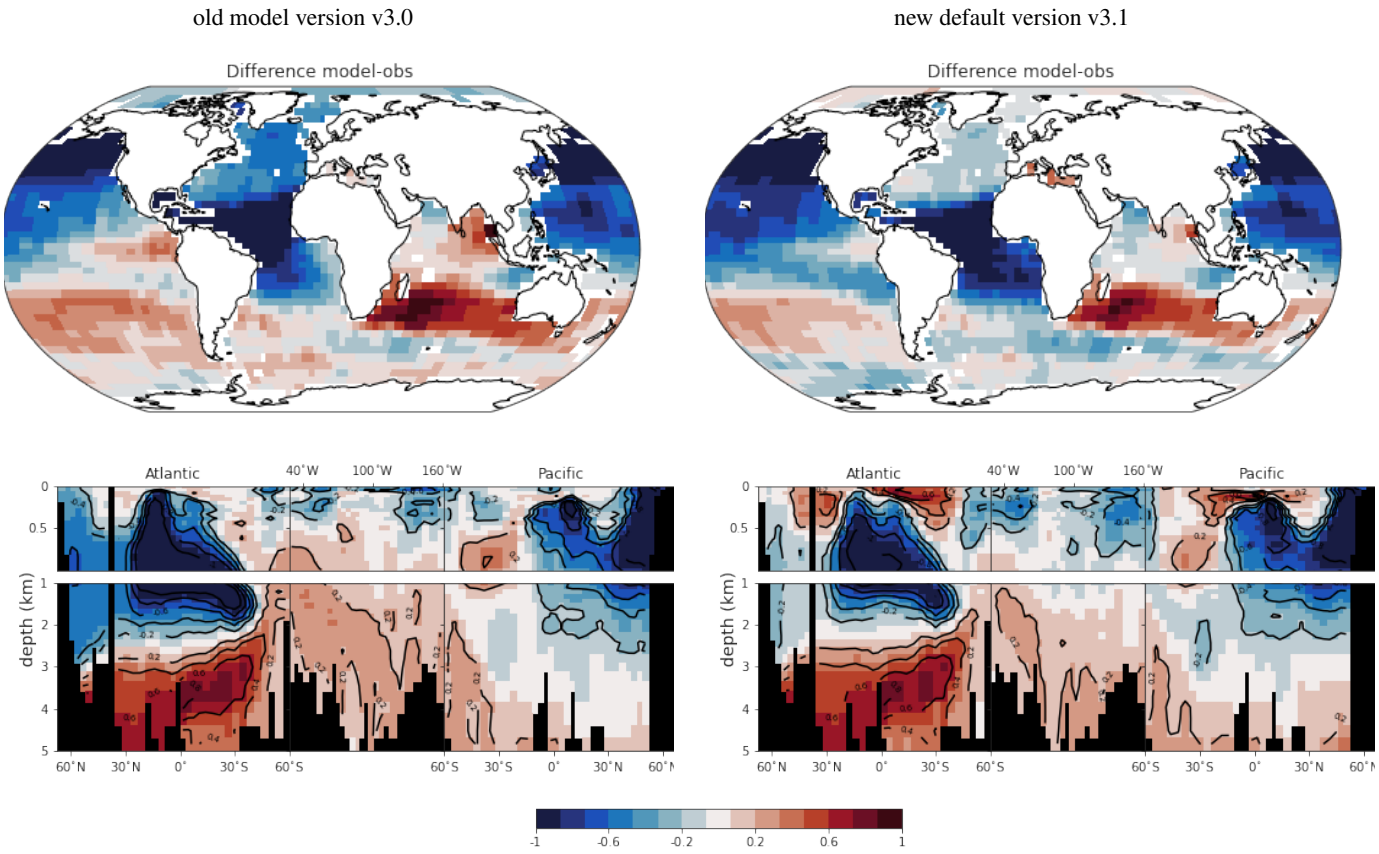

Figure S2.18. Model error of PO_4 concentrations (mmol/m^3) at 750 m depth and in a transect through three ocean basins in the old and new default model versions.

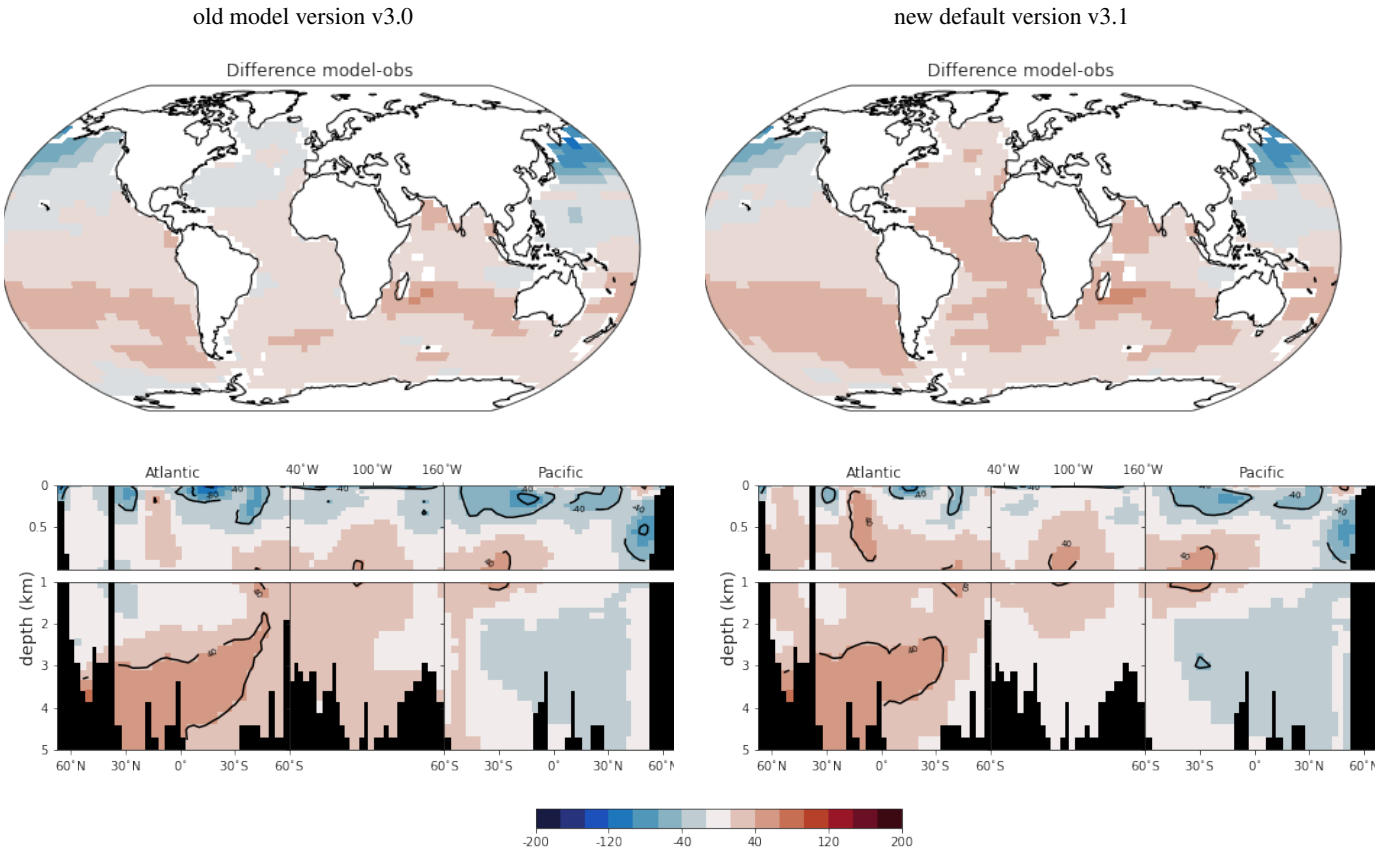

Figure S2.19. Model error of ALK concentrations (mmol/m^3) at 750 m depth and in a transect through three ocean basins in the old and new default model versions.

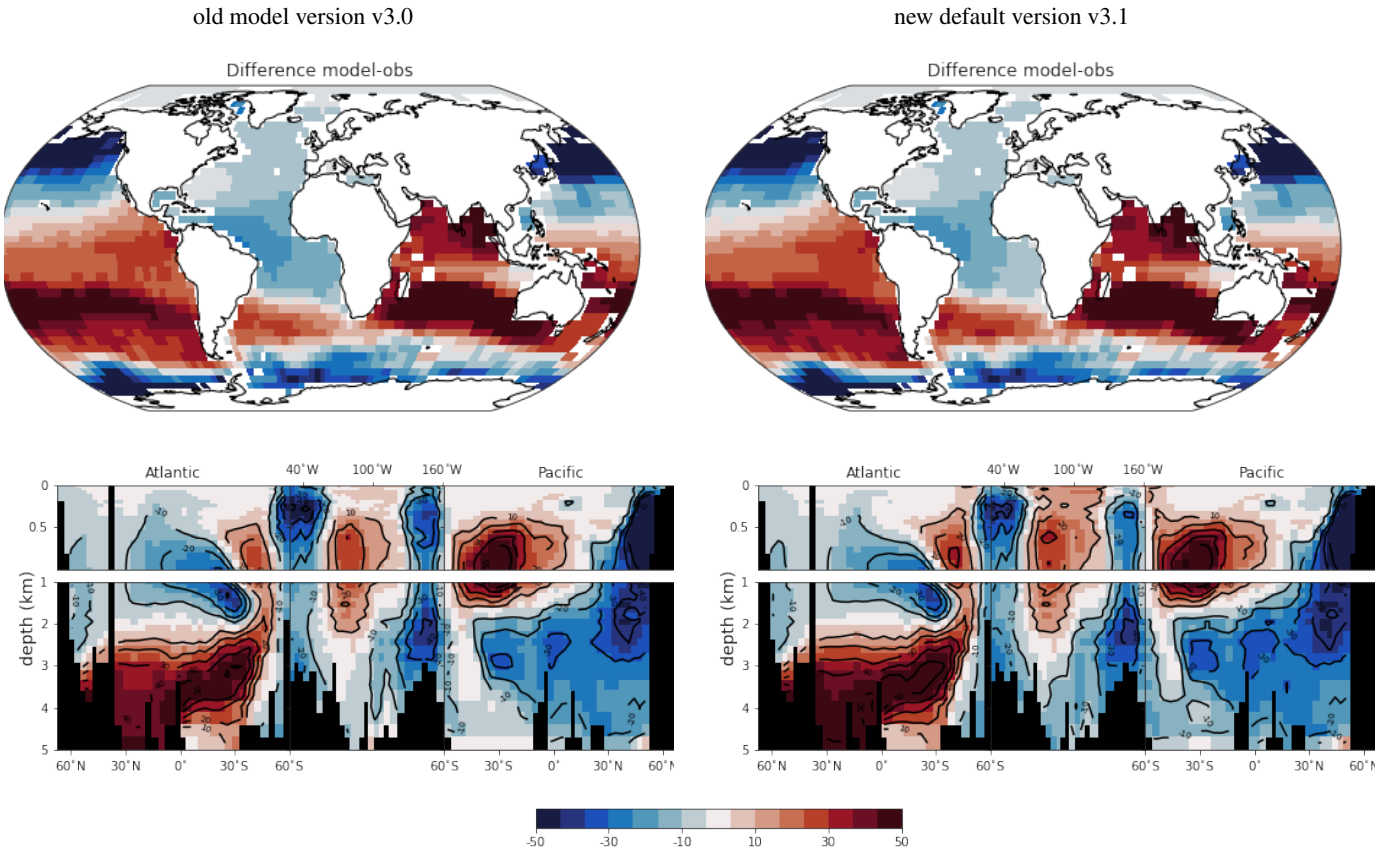

Figure S2.20. Model error of SiO concentrations (mmol/m^3) at 750 m depth and in a transect through three ocean basins in the old and new default model versions.

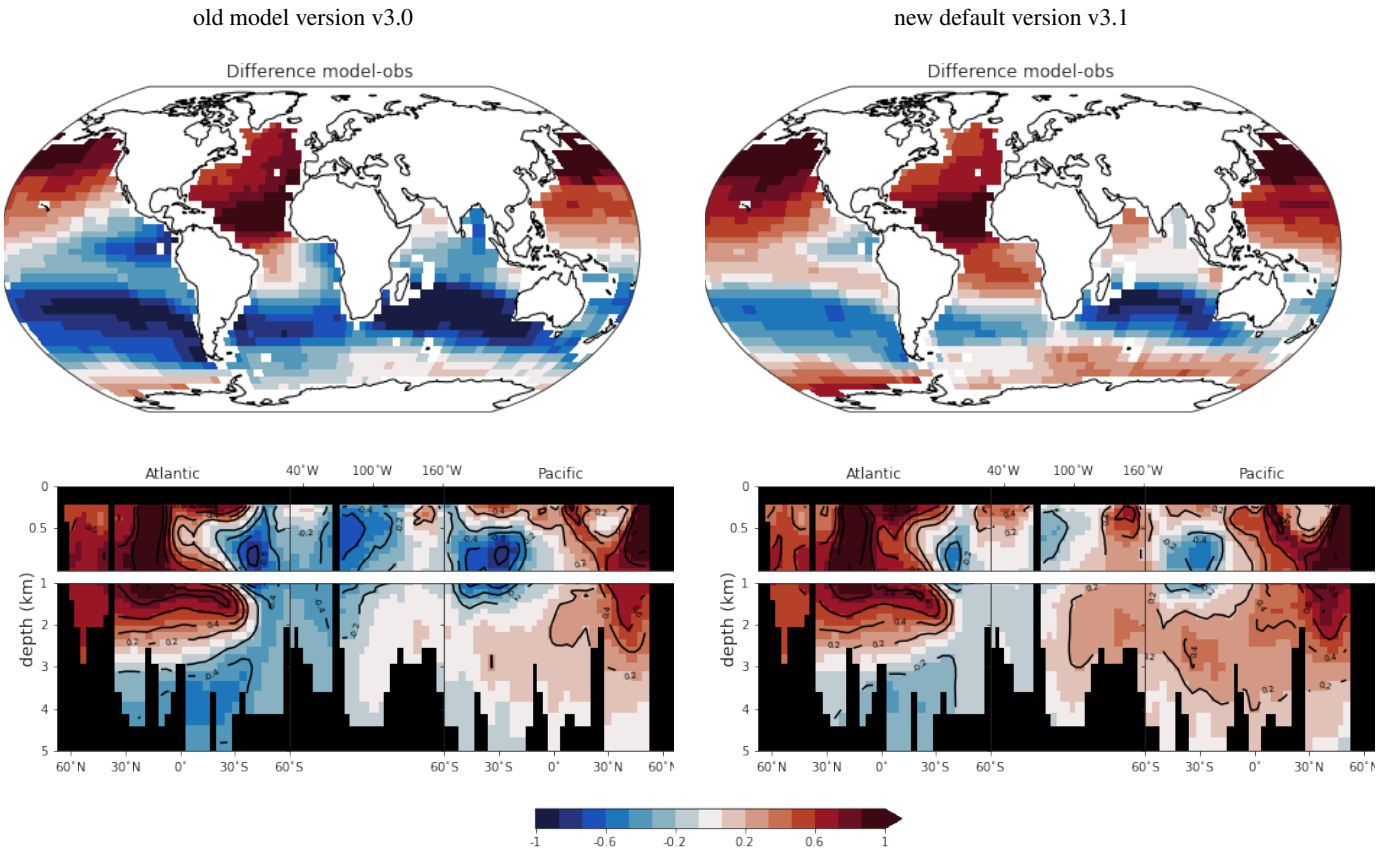

Figure S2.21. Model error of δ^{13}C (‰) of DIC at 750 m depth and in a transect through three ocean basins in the old and new default model versions.

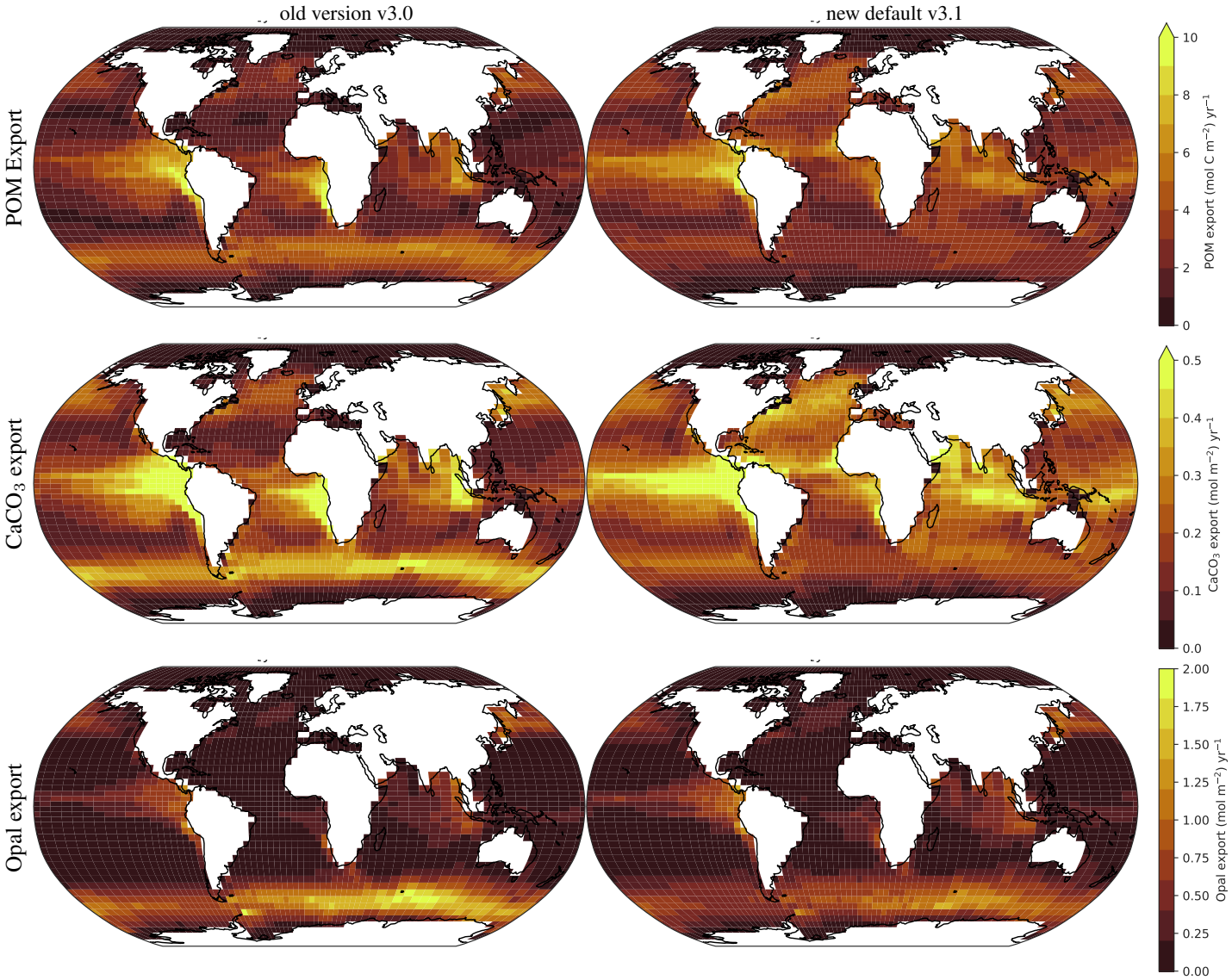

Figure S2.22. Simulated export fields in the old model version (left column) and new default version (right column).